TRIUMF

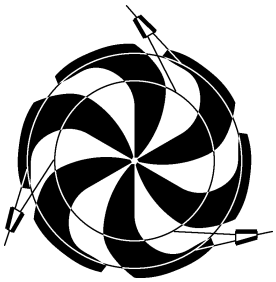

ANNUAL REPORT
SCIENTIFIC ACTIVITIES
2005

ISSN 1492-417X

CANADA'S NATIONAL LABORATORY FOR PARTICLE AND NUCLEAR PHYSICS

OPERATED AS A JOINT VENTURE

MEMBERS:

THE UNIVERSITY OF ALBERTA
THE UNIVERSITY OF BRITISH COLUMBIA
CARLETON UNIVERSITY
SIMON FRASER UNIVERSITY
THE UNIVERSITY OF TORONTO
THE UNIVERSITY OF VICTORIA

ASSOCIATE MEMBERS:

THE UNIVERSITY OF GUELPH
THE UNIVERSITY OF MANITOBA
McMASTER UNIVERSITY
L'UNIVERSITÉ DE MONTRÉAL
QUEEN'S UNIVERSITY
THE UNIVERSITY OF REGINA
SAINT MARY'S UNIVERSITY

UNDER A CONTRIBUTION FROM THE
NATIONAL RESEARCH COUNCIL OF CANADA

DECEMBER 2006

The contributions on individual experiments in this report are outlines intended to demonstrate the extent of scientific activity at TRIUMF during the past year. The outlines are not publications and often contain preliminary results not intended, or not yet ready, for publication. Material from these reports should not be reproduced or quoted without permission from the authors.

PARTICLE PHYSICS

Experiment 614
TWIST – the TRIUMF weak interaction symmetry test

(R.P. MacDonald, Alberta; G.M. Marshall, TRIUMF)

This has been an exciting year for the TWIST (TRIUMF weak interaction symmetry test) collaboration. The year saw the publication of our first physics results [Musser *et al.*, Phys. Rev. Lett. **94**, 101805 (2005); Gaponenko *et al.*, Phys. Rev. **D71**, 071101(R) (2005)] and a detailed description of the detector system [Henderson *et al.*, Nucl. Instrum. Methods **A548**, 306 (2005)] that was constructed at TRIUMF. In addition, TWIST has made a number of major improvements in hardware, software, and techniques, and acquired new, higher-quality data for the next round of measurements.

TWIST is an experiment to measure the muon decay spectrum, to extract the precise values of three of the four decay (Michel) parameters. If the results differ from the standard model prediction, the deviations indicate contributions from physics beyond the standard model. The goal of TWIST is to simultaneously determine these decay parameters with experimental precision better than 10^{-3}, to eventually achieve an approximately tenfold improvement on the precision of previous experiments. When this goal is met, it will set new limits on the right-handed coupling of the muon in a model independent way, as well as squeeze the parameter space for certain classes of extensions to the standard model.

Using data acquired in late 2002, TWIST completed its first round of measurements of the decay parameters ρ (rho) and δ (delta). We developed a better understanding of the systematics involved in the measurement, especially through "exaggeration" studies where a systematic effect is exaggerated to measure its impact on the decay parameters. A large amount of data – 6 billion muon decays, plus equivalent Monte Carlo – was analyzed for the parameter measurements and systematics studies, a feat made possible by the new WestGrid computing cluster located at UBC, available for the first time this year. TWIST's first physics publication reported that the decay parameter ρ [Musser *et al., op. cit.*] was measured to be $0.75080 \pm 0.00032(\text{stat}) \pm 0.00097(\text{syst}) \pm 0.00023$, where the last uncertainty represents the dependence of ρ on the Michel parameter η (eta). The ρ parameter determines the momentum dependence of the isotropic part of the decay distribution. A detailed description of the analysis formed the Ph.D. dissertation of Jim Musser. In a second publication [Gaponenko *et al., op. cit.*], the parameter δ was reported to be $0.74964 \pm 0.00066(\text{stat}) \pm 0.00112(\text{syst})$; δ is a measure of the momentum dependence of the anisotropic distribution in polarized muon decay. That analysis was described in detail in the Ph.D. dissertation of Andrei Gaponenko. Both measurements are consistent with the standard model values of ρ and δ (3/4 in both cases).

Using the experience from this analysis, TWIST has continued development for the next round of measurements. Many improvements in hardware, software, detector control systems, etc. continued through 2005. Late in 2004, new data were taken under better-controlled conditions, which should result in lower systematic uncertainties for measurements of ρ and δ. A comparison with the standard model prediction of the muon decay spectrum was also carried out to search for anomalous two-body decay modes of the muon into a positron plus a single undetected neutral particle, rather than neutrinos. No signal was observed, but more stringent limits for the process were set, and the analysis formed the M.Sc. thesis of Ryan Bayes [University of Victoria (2005)].

An analysis was completed in 2005 that provided TWIST's first direct measurement of another decay parameter, ξ, in terms of the product $\mathcal{P}_\mu\xi$, where $\mathcal{P}_\mu$ is the muon polarization. Since the muon decay formula cannot in principle distinguish between variations in $\mathcal{P}_\mu$ and ξ separately, the main difficulty is to understand and evaluate all processes that could affect the polarization from the time the muon is produced in pion decay. In the standard model, neglecting neutrino masses, $\mathcal{P}_\mu$ is 100% (anti)parallel to the muon momentum when the muon is produced, but subsequent multiple scattering and other interactions with materials can reduce this number. In addition, the fringe field of the TWIST solenoid changes the distribution of directions of muon momenta, leading to an apparent reduction of $\mathcal{P}_\mu$ by the time the muon decays. These and other effects can lead to systematic uncertainties that require careful evaluation prior to comparison of $\mathcal{P}_\mu\xi$ with the standard model prediction. The challenges and their solutions are documented in the Ph.D. thesis of Blair Jamieson [University of British Columbia (2005)]. A publication of the results is in preparation.

The TEC, or time expansion chamber, is an instrument placed in the beam line at the entrance to the TWIST spectrometer, to measure the properties of the incoming beam. Operated for the first time in 2004, it was used extensively during 2005 for beam studies, especially in order to understand the way the muon beam passed through the fringe field of the spectrometer. An instrumentation paper is in preparation

describing TEC construction, operation, and application to TWIST data analysis.

The TEC is the major tool in TWIST's assessment of the effect of the fringes of the solenoidal magnetic field on depolarization. Although there was an "engineering" component to the use of the TEC this year, to learn how to align, calibrate, and operate it effectively, at the same time it was used successfully to improve the understanding of the muon beam. This resulted in better consistency of the beam properties between data sets and provided a more realistic description of the muon beam for input into the Monte Carlo simulation. Figure 1 is a measurement of the beam profile near the entrance to the solenoid but prior to the strongest radial fringe field components. It shows the intensity of the beam as a function of horizontal (x) and vertical (y) dimensions. Note that the beam position is displaced vertically; this is caused by the fringe field of the 2 T solenoid that extends into the final dipole and quadrupoles of M13. Vertical steering must be added to the beam line to compensate for the displacement. The TEC measures the angles of particles as well as their positions. Figure 2 shows the distribution of angles projected to the horizontal plane (θ_x), while Fig. 3 shows the distribution for the vertical projection (θ_y), for the beam profile of Fig. 1. The rotation of the beam due to the solenoid fringe field is shown, especially in Fig. 3, from the gradients. The TWIST Monte Carlo simulation uses as input all three distributions as determined for each of several data sets.

New monitoring techniques were developed that improved the quality of the data. The change in shape and position of drift chamber foils due to temperature

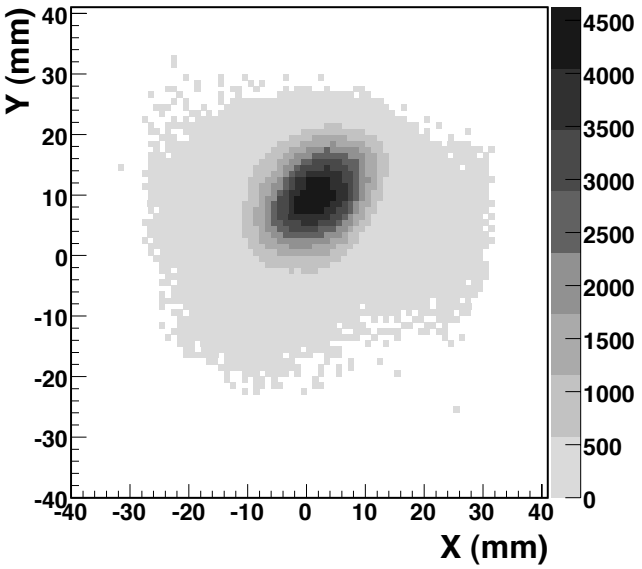

Fig. 1. Two-dimensional distribution of the muon beam intensity at the TEC, near the fringe field region of the TWIST spectrometer. The pixel size in the figure is 1×1 mm^2.

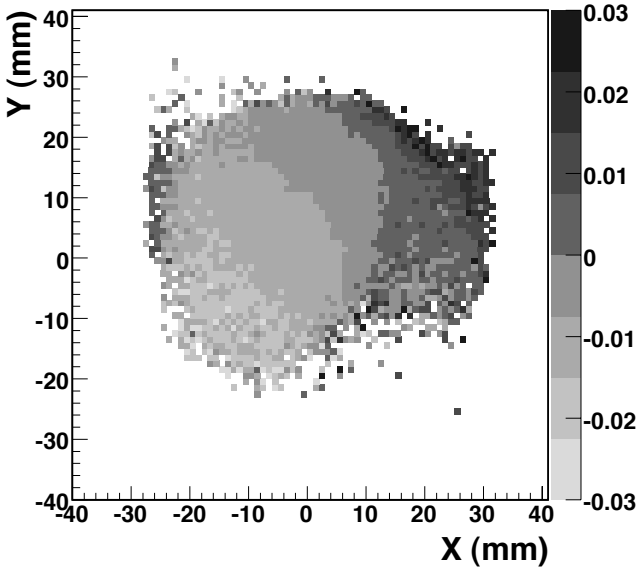

Fig. 2. Two-dimensional distributions of the muon beam mean angle projected to the $y = 0$ (horizontal) plane (θ_x) for the beam intensity distribution shown in Fig. 1. The gray scale represents the angles in radians.

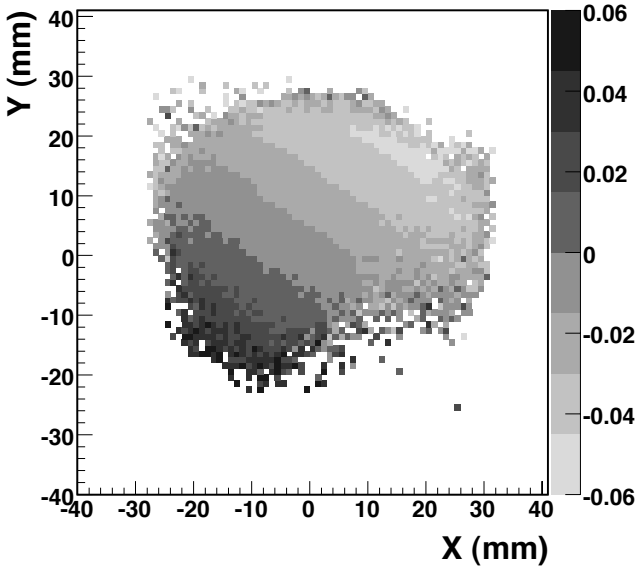

Fig. 3. Similar to previous figure, but projected to the $x = 0$ (vertical) plane (θ_y). The gray scale is different to show the trends more clearly.

and pressure variations was monitored and controlled, greatly reducing fluctuations in the drift times in the chambers. The muon stopping position was regulated to keep it centred within the stopping target despite changes in gas density (due to atmospheric changes). The alignment of the entire detector to the magnetic field was measured and taken into account in the analysis.

Improvements in the Monte Carlo simulation were developed as well. More accurate drift chamber cell geometry was implemented. As mentioned above, a

more realistic muon beam description was used, made available by the TEC. Through specialized data sets, a better understanding was achieved of how well the positron hard interactions are simulated.

With experience gained in 2005, both through the analysis of data from 2004 and from continued operation of the TWIST spectrometer and the TEC, the TWIST group remains confident that the original goals of the collaboration can be achieved. Improvement of the precision of measurements of ρ, δ, and $\mathcal{P}_\mu\xi$, by at least one order of magnitude compared to previous experiments, appears to be attainable.

The ATLAS Experiment at the LHC
(C. Oram, I. Trigger, TRIUMF)

As described in detail in the 1996 Annual Report, ATLAS is building a general purpose *pp* detector which is designed to exploit the full discovery potential of the Large Hadron Collider (LHC) at CERN. The TRIUMF group is responsible for the management and engineering of the hadronic endcap (HEC) calorimeters, and the transport of the two 280 ton endcap cryostats to the ATLAS pit. This year has seen the completion of these tasks.

The TRIUMF group has been significantly enlarged this year with Isabel Trigger and Reda Tafirout becoming TRIUMF scientists, and Yoshio Ishizawa being hired as a post-doctoral fellow. The TRIUMF group has been active in preparations for analysis of initial data and with the Canadian universities on the development of a computer hub to process ATLAS data. The computing developments are discussed elsewhere in this Annual Report.

The ATLAS detector installation in the pit is well advanced. Figure 4 shows the detector on November 4, with the eight coil toroid magnet installation completed and the barrel calorimeter about to be moved to the centre of the detector. The installation of the LHC is progressing well with the critical path item magnet installation progressing well. The magnet installation rate is presently close to 20 per week, with more than 200 of the approximately 1200 installed. This, together with interconnect work, is anticipated to remain the main bottleneck until the end of installation.

Physics goals

The present theoretical understanding of elementary particles is in the context of the standard model. It

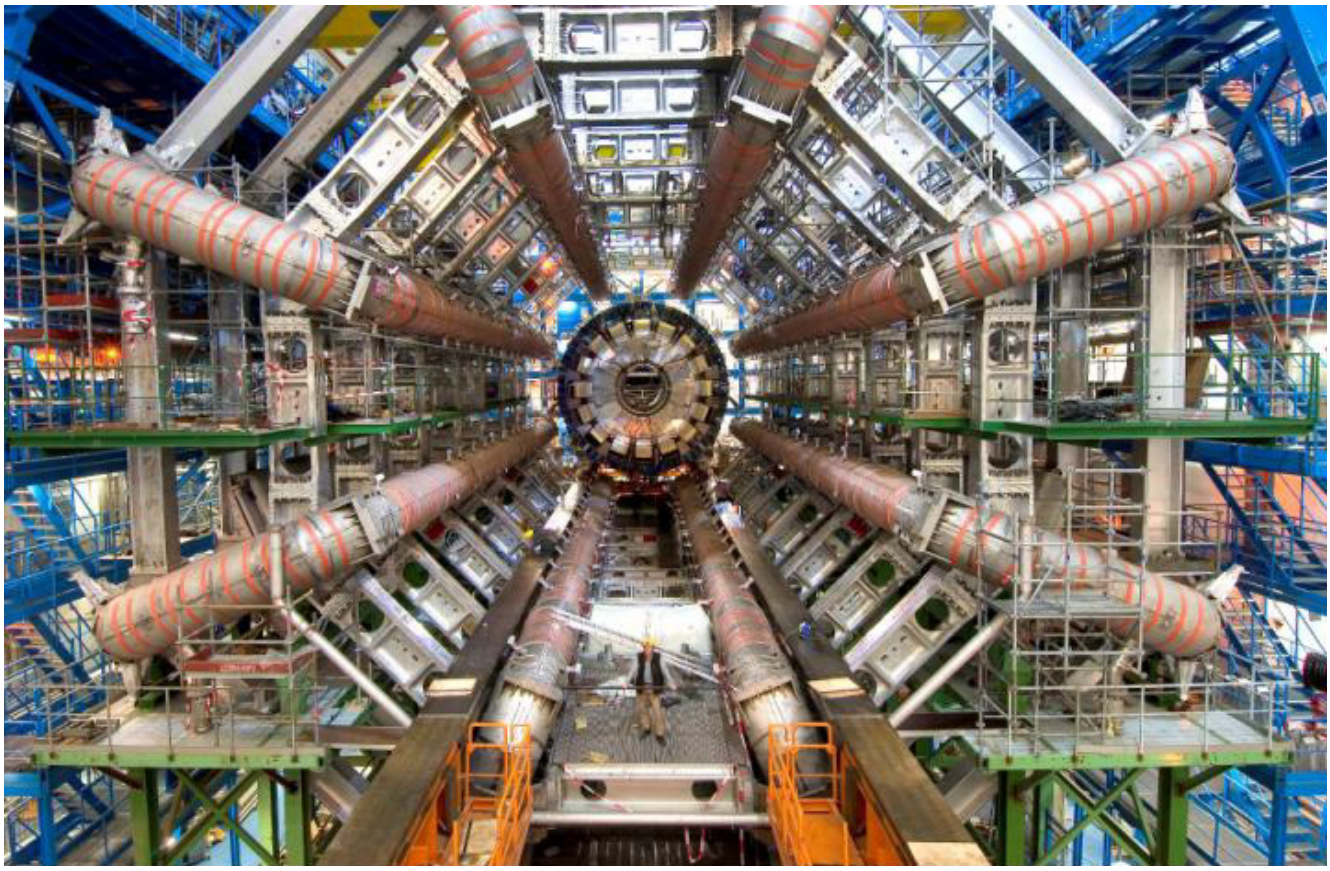

Fig. 4. The ATLAS detector during installation. This picture was taken on November 4, 2005, just prior to the successful movement of the barrel calorimeter (seen in the centre of the picture) to its final location in the centre of the eight toroid coils of the barrel muon system.

is a remarkably successful model, its predictions having been consistently confirmed by experiments for over three decades. Its agreement with experimental results, to enormous accuracy in some cases, makes it arguably the most accurately verified model in science.

Of the many elementary particles contained in the standard model, only one remains to be discovered: the Higgs boson, a spinless particle which is required by the spontaneous symmetry-breaking mechanism in the electroweak sector. Electroweak symmetry breaking generates the masses of the gauge bosons and also allows the fermions that make up the fundamental matter of the universe to acquire mass. It is thus related to one of the most fundamental questions of physics: What is the origin of the different particle masses? New direct experimental insight is required to answer this question.

The simplest manifestation of the spontaneous symmetry-breaking mechanism would be the existence of a standard model Higgs boson (H), but many more plausible models predict multiple Higgs particles. For example, in the minimal supersymmetric extension of the standard model (MSSM), there are five Higgs: ($H^{\pm}$, h, H and A).

There are good theoretical reasons to believe that the discovery of the Higgs will be accompanied by hints of, and more likely direct evidence for, what lies beyond the standard model. In the standard model, which is a highly nonlinear dynamical system, the elementary particles tend to take on the heaviest of all possible mass scales, which in such a model are at inaccessible energies and inconsistent with other requirements of the model. All other particles discovered thus far have natural mechanisms, such as gauge and chiral symmetries, for protecting their masses so that they can lie in the observable range. For the Higgs particle, there is no such symmetry in the present model.

Theoretical scenarios which leave the Higgs particle light enough to be observed include technicolour, supersymmetry and other models invoking extra dimensions in which gravity can propagate with a strength comparable to the nuclear and electromagnetic forces. If a Higgs is observed at the LHC, its mass, spin properties and couplings should begin to elucidate the nature of the physics beyond the standard model. If the Higgs is composite, its existence requires as yet unknown ultra-strong forces. If it is elementary, it would be the only spinless particle to be discovered so far.

There is a theoretical "naturalness" problem for the masses of spinless particles. The present theoretical view is that the conventional grand unification of the strong, weak and electromagnetic forces can only work in the supersymmetric extension of the standard model. In that model, the grand unified energy scale is only two decades below the Planck scale, the ultimate energy where space-time itself has quantum fluctuations. It is not out of the realm of imagination that, at energy scales where supersymmetry would be observed, evidence for an ultimate theory of everything, or at least everything that can exist once space-time is formed, might be within human grasp.

The central goal of ATLAS is the search for the Higgs, or Higgs-like particles. Whatever the precise nature of the mechanism by which electroweak symmetry is broken, new particles, including at least one which must play the role of the Higgs, are expected in the TeV-energy region. Experiments at the LHC, where the ATLAS detector will take data, will probe this energy region. This will be the first experimental probe in many years of an energy region where fundamentally new physics is definitely expected to occur. There is every reason to believe that the results will be among the most dramatic ever.

The Higgs search was used as a first benchmark for the detector optimization, and can now serve us again as a benchmark for initial analysis design. For the SM Higgs, the detector is sensitive to the following processes ($\ell = e$ or μ) in order to cover the full mass range above the discovery limit set by the final LEP operation in the fall of 2000:

- $H \to b\bar{b}$ from WH, ZH and $t\bar{t}H$ using a $\ell^{\pm}$ and b-tagging,
  mass range $80 < m_H < 100$ GeV,
  this requires good lepton reconstruction, a solid understanding of b-tags and a measurement of the jet-energy scale for jets with heavy flavours;
- $H \to \gamma\gamma$
  mass range $90 < m_H < 150$ GeV,
  this requires excellent calibration of the electromagnetic calorimeters;
- $H \to WW^* \to \ell^{\pm}\nu\ell^{\pm}\nu$
  mass range $150 < m_H < 200$ GeV,
  this and the two following scenarios require good lepton reconstruction and the ability to measure missing transverse energy in the calorimeters;
- $H \to ZZ^* \to 4\ell^{\pm}$
  mass range 130 GeV $< m_H < 2m_Z$;
- $H \to ZZ \to 4\ell^{\pm},\ 2\ell^{\pm} + 2\nu$
  mass range $m_H > 2m_Z$;
- $H \to WW,\ ZZ \to \ell^{\pm}\nu + 2$ jets, $2\ell^{\pm} + 2$ jets
  from WW, ZZ fusion using tagging of forward jets for m_H up to about 1 TeV,
  this requires an excellent calibration of the jet-energy scale in the forward calorimeters, and good reconstruction of leptons and missing transverse energy.

In addition to signatures similar to these, the MSSM Higgs searches also require sensitivity to pro-

cesses such as:

$$A \to \tau^+\tau^- \quad \to \quad e\mu + \nu\text{'s}$$
$$\to \quad \ell^\pm + \text{hadrons} + \nu\text{'s};$$

$$H^\pm \quad \to \tau^\pm\nu \quad \text{from } t\bar{t} \to H^\pm W^\mp b\bar{b} \text{ and}$$
$$\to 2 \text{ jets} \quad \text{using a } \ell^\pm \text{ tag and } b\text{-tagging.}$$

In supersymmetric scenarios, we expect to observe not only Higgs bosons, but also many new supersymmetric partners of the fermions. These typically decay in cascades, ending with a stable lightest supersymmetric particle (LSP) which interacts only weakly with the detector and thus escapes undetected. Supersymmetric signatures therefore consist of jets, leptons and, most crucially, missing transverse energy from the escaping LSP.

The observable cross sections for most of these processes are small over a large part of the mass range to be explored at the LHC. Hence it is important to operate at high luminosity, and to maximize the detectable rates above backgrounds by high-resolution measurements of electrons, photons, and muons. Initial analysis design focuses on simple, cut-based selections which will help us to calibrate the jet-energy scale, understand the calorimeter resolutions, and eventually measure missing transverse energy.

The possible signatures of new particles from physics processes beyond the standard model are many and various, which is why ATLAS is such a large and complicated detector. In general, though, most Higgs-like particles will have decays to b-quark jets or to photons that require an excellent understanding of the calorimeters, and most supersymmetry-like signatures involve missing transverse energy, which can only be measured if the jet response and electromagnetic response of the calorimeters are well understood.

Figure 5 shows the estimated signal significance for the standard model Higgs discovery in ATLAS over the presently theoretically favoured region: 100–200 GeV/c^2. From 100–190 GeV/c^2, the most significant discovery channels are those where the Higgs is produced by vector boson fusion [see Asai *et al.*, "Prospects for the search for a standard model Higgs boson in ATLAS using vector boson fusion", ATLAS Note SN-ATLAS-2003-24]. While the production cross section is lower in these channels, the ability to cleanly tag the Higgs production using forward jets that enter the endcap calorimeters more than compensates, yielding superior signal to noise. The need to use the endcap calorimeters for this tag puts a premium on obtaining an early robust calibration for the calorimeters over the entire angular range.

The TRIUMF group is well placed to be in the front lines of the discovery effort: we have extensive

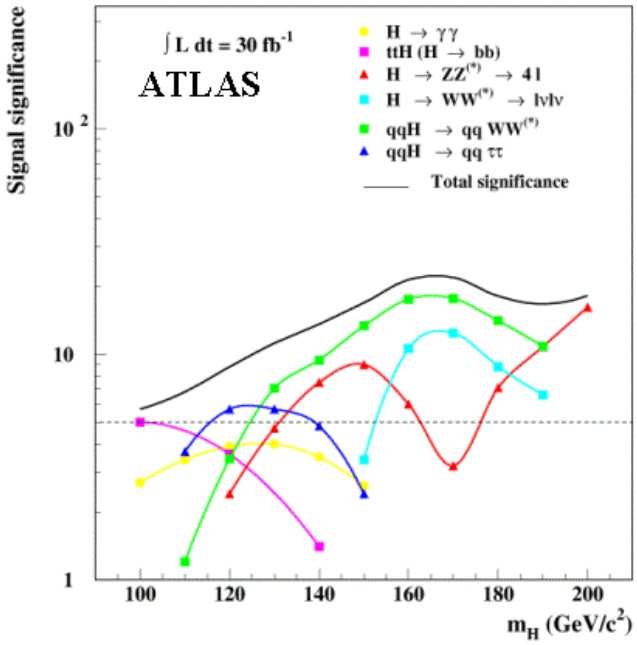

Fig. 5. ATLAS sensitivity for the discovery of a standard model Higgs boson for an integrated luminosity of 30 fb^{-1}. The signal significances are plotted for individual channels, as well as for the combination of all channels.

calorimetry expertise, and we have the computing expertise needed for efficient access to the data. A significant portion of the ATLAS hadron calorimeter system was designed and built at TRIUMF. Hence we are making an effort to focus our initial analysis efforts around understanding the jet-energy scale (in events consisting of Z bosons and jets) and making sure that there is adequate validation of hadronic reconstruction. We can then move on to studies of topologically similar events consisting of associated production of a Z boson and a Higgs boson decaying to jets. We are also interested in vector boson fusion, simple top quark mass measurements and Higgs production in supersymmetry cascades, all of which fit into this program of calorimeter-intensive studies which can be done with the first few months' data from the LHC.

We make a conscious effort to exercise local computing resources, with a view to increasing our local technical expertise. We have tried to centralize local ATLAS software at TRIUMF, to minimize time spent by individual physicists on installing new software releases. We use the LCG GRID resources to access centrally produced Monte Carlo simulated data files. We use WestGrid facilities to generate our own simulated data, and are thinking about using WestGrid for some of our large analysis tasks, so that we can use the GRID resources more directly.

The TRIUMF ATLAS physics group is expected to be an analysis resource for other physicists working

in Canada (and perhaps to some extent on the West Coast of the USA). We are therefore making considerable efforts to document how to do analysis in Canada, and to provide a local supplement to the documentation available at CERN, so that a new student or postdoc can begin to be productive in a minimum amount of time. We are also trying, as equipment permits, to set up our resources and analyses in "official" ATLAS ways. Finally, we have begun to participate in regular weekly meetings with our colleagues at the Universities of Victoria and British Columbia, and Simon Fraser University, where we discuss analysis and commissioning work in progress. We will be hosting a Canada-wide ATLAS physics analysis meeting at TRIUMF in April, 2006.

Canada's participation in ATLAS

The Canadian group consists of about 35 grant eligible physicists from TRIUMF, University of Alberta, Carleton University, Simon Fraser University, University of British Columbia, Université de Montréal, University of Toronto, University of Victoria, McGill University, and York University. We have been strongly involved in three construction projects centred around detecting hadrons in the endcap region: the hadronic endcap project, the hadronic portion of the forward calorimeter project, and the pipeline electronics for calorimetry. In addition, as part of our common project contribution, we delivered the cryogenic signal feedthroughs for the two liquid argon endcap cryostats. These construction projects are now essentially completed, although much is left to be done to commission the calorimeter systems in the ATLAS pit. In the coming year the cryostats will be cooled down and systems made ready for first beams in mid-2007. TRIUMF is also centrally involved in the detector control system (DCS) for the liquid argon calorimeters, and provides the convener for this project. In ATLAS management Chris Oram is the ATLAS Collaboration Board Chair (see the ATLAS organization chart at http://atlas.web.cern.ch/Atlas/-Management/Organization.gif). He sits *ex-officio* on the ATLAS executive board and is consulted on all major ATLAS appointments.

The hadronic endcap project

The hadronic endcap (HEC) calorimeter is a liquid argon sampling calorimeter with copper absorbers [ATLAS Collab., ATLAS Liquid Argon Technical Design Report (1996)]. A concise overview of this design was provided in the 1996 TRIUMF Annual Report. The construction is now complete, and the detectors installed in the two endcap cryostats. Four detector systems sit in each endcap cryostat: the presampler is closest to the interaction region and is followed by the electromagnetic endcap calorimeter (EMEC) and the HEC. At the inner diameter, the forward calorimeter (FCAL) is installed around the beam pipe. These calorimeters form the endcap calorimeter system. A paper is in preparation describing the HEC calorimeter and associated systems as installed. We anticipate this will be published in a journal such as NIM during 2006.

Endcap calorimeter system This year the second, and final, endcap was successfully cold tested. Both endcap calorimeter systems, having been fully cold tested, were transported to the ATLAS pit (Fig. 6). This transport was planned by Roy Langstaff (TRIUMF), who also arranged with CERN civil engineering staff for widening of the road. The transport proceeded successfully, and was filmed as part of a documentary on ATLAS by the Canadian Discovery Channel. One endcap has been lowered to the pit, the other awaits lowering in early 2006. The emphasis of the work has now shifted to commissioning of the equipment in the ATLAS pit.

Test beam measurements of the hadronic endcap modules In 2004 we undertook the joint test of the three calorimeters in the endcap. An engineering run of the test beam set-up was undertaken in February, 2004, with beam runs in the spring and fall of 2004. This test of the EMEC, HEC and FCAL was successful, and analysis of results is ongoing. This region is complicated as it has a physically complex overlap between the 3 detectors which includes significant dead material. These tests are important as they form the basis of the initial calibration of the calorimeter, and test techniques that can be employed to extend the calibration in this complex region to the highest shower energies anticipated from collisions at the LHC.

Fig. 6. Transport of the second endcap calorimeter in its cryostat to the ATLAS pit.

The detector control system (DCS) The DCS system in the liquid argon calorimeter system covers all aspects of the calorimeter that must be monitored and controlled. These include: the argon purity and temperature, the HV on the calorimeters, and the various voltages on the front end crates. This system is a responsibility of the TRIUMF ATLAS group. During this year significant progress has been made on this system, much of which was used in the cold tests of the cryostats prior to transport to the pit.

Test beam measurements of the hadronic endcap at sLHC intensities While we have yet to start taking data with the ATLAS calorimeters, CERN has announced that it intends to push the intensity of the LHC an order of magnitude beyond the nominal maximum LHC intensities in an upgrade that would create a machine called the super LHC (sLHC). The timescale of this upgrade is about 2012. The intensities of the sLHC will create a challenge for the ATLAS endcap liquid argon calorimetry. The HEC calorimeter will move into an operational mode, in the forward region, where the charge resident on the plates that form the HEC calorimeter will be less than the positive charge of the ions in the liquid argon between the plates. No calorimeter has been operated in this mode. Predictions of how the calorimeter will operate are hampered by knowledge of such things as the positive ion mobility and the charge recombination rate. Tests are being planned to run a test cell in an intense 60 GeV proton beam (10^9 particles per second) to simulate this situation. The TRIUMF group is involved in the specification of these tests, including the required proton beam pulse structure and the design of the mechanical and electronic equipment.

BNL 787/949/KOPIO
Search for rare kaon decays $K \to \pi\nu\bar{\nu}$

(D. Bryman, UBC; T. Numao, TRIUMF)

Precise measurements of rare muon, pion, and K meson decays which have precise standard model (SM) predictions, enable exacting tests of current theories and searches for new physics at extremely high mass scales. Prominent among such processes are the branching ratios B($K^+ \to \pi^+\nu\bar{\nu}$)and B($K_L^0 \to \pi^0\nu\bar{\nu}$) which are among the most incisive measurements possible in the study of CP violation (CPV) and quark mixing, uniquely allowing direct access to the SM CPV phase. $K \to \pi\nu\bar{\nu}$ reactions are flavour-changing neutral current processes, arising at the one loop level in the SM. The presence of the top quark in the loops makes these decays very sensitive to the elusive CKM coupling V_{td}. This sensitivity can be fully exploited because of the hard GIM suppression, the relatively small QCD corrections (calculated to next-to-leading-logarithmic order), and the fact that the hadronic matrix element can be determined to a few per cent from the rate of $K \to \pi e\nu$ (K_{e3}) decay. In the SM, the branching ratios are expected to be B($K^+ \to \pi^+\nu\bar{\nu}$) = $(7.9 \pm 1.2) \times 10^{-11}$ and B($K_L^0 \to \pi^0\nu\bar{\nu}$) = $(2.9 \pm 0.4) \times 10^{-11}$. Long distance contributions are known to be negligible so not only can the effects of SM short-distance physics be clearly discerned but also the effects of possible non-SM physics, for example, in the minimal supersymmetric SM and in R-parity violating supersymmetry. With present limits on supersymmetric parameters, SUSY can give a contribution of 50% as large as the SM component for B($K^+ \to \pi^+\nu\bar{\nu}$) and therefore has to be taken into account. Much larger effects can occur for B($K_L^0 \to \pi^0\nu\bar{\nu}$). It is notable that the effects of SUSY on the K and B system generally turn out to be discernibly different. Discovery and study of these reactions were the main focus of BNL experiments E949 and KOPIO. E949 acquired a significant data set but, unfortunately, the RSVP project which included KOPIO was abruptly terminated by the NSF.

E949 at BNL

Measurement of $K^+ \to \pi^+\nu\bar{\nu}$ decay from kaons at rest involved observation of the π^+ in the momentum region $211 < P < 229$ MeV/c ("PNN1": above the $K^+ \to \pi^+\pi^0$ ($K_{\pi 2}$) peak) in the absence of other coincident activity. Primary background sources were pions from the two-body decay $K_{\pi 2}$, muons from $K^+ \to \mu^+\nu$ ($K_{\mu 2}$) and other decays, pions scattered from the beam, and charge exchange reactions followed by $K^0 \to \pi^+\ell^-\nu$, where $\ell = e$ or μ. E949 took data in 2002 and substantial results have been published including discovery of the third $K^+ \to \pi^+\nu\bar{\nu}$ event and measurements of other rare processes.

We are now pursuing analysis of E949 $K^+ \to \pi^+\nu\bar{\nu}$ data to study the lower momentum phase space region ("PNN2": $P < 205$ MeV/c) below the $K_{\pi 2}$ peak which has the potential to double the sensitivity of the experiment. The lower energy region is also more sensitive to certain non-SM effects such as scalar interactions. The background is dominated by $K_{\pi 2}$ decays in which the π^+ is initially emitted along the beam axis and scattered in the target into the solid angle; the direction of the γs from the $\pi^0 \to \gamma\gamma$ decay will also tend to be at small angles to the beam axis. Events would be accepted as signal if the scatter in the target goes undetected and the γs from the π^0 decay are missed by the PV detector. Identification of events which scattered in the target can be accomplished by detailed analysis of the pulse shapes recorded from the target fibres using the 500 MHz CCD transient digitizer data for decay times >6 ns following the K^+ stop. To increase the

PV rejection in the PNN2 region, the present analysis makes use of information from several new or upgraded sub-detectors (active degrader, collar, upstream veto, and downstream veto) intended specifically to enhance the detection of small angle photons from scattered events. In addition, the new barrel veto liner added 2.4 radiation lengths (X_0) in the barrel region.

For the present analysis, a new tag for scattered events was developed, based on recognizing kinks in the target portions of the outgoing tracks of scattered pions. This tag is expected to be efficient enough to provide a large sample of scattered events to tune the cuts.

In addition, we have used E949 data to study improvements in photon detection efficiency relevant to measurements of $K \to \pi\nu\bar{\nu}$, search for several other non-SM processes (e.g. $\pi^0 \to \nu\bar{\nu}$ with a 90% c.l. upper limit of 2.7×10^{-7}), and study important radiative K decays including $K^+ \to \pi^+\gamma\gamma$ with a 90% c.l. upper limit of 8.3×10^{-9} for the region $P > 213$ MeV/c, $K^+ \to \pi^0\mu^+\nu\gamma$, and $K^+ \to \pi^+\pi^0\gamma$.

KOPIO

The preradiator (PR) was at the heart of the KOPIO signal detection technique designed to efficiently measure the position, angle, time, and energy of photons from $K_L^0 \to \pi^0\nu\bar{\nu}$ decay. The detection system for $\pi^0 \to \gamma\gamma$ decay allowed a fully constrained reconstruction of the decay vertex, and mass, energy, and momentum measurements in the K_L^0 centre of mass system obtained using time-of-flight techniques. This was accomplished by accurately measuring the position of interaction, angle, and energy of each individual photon in a fine grained PR detector followed by an efficient calorimeter. The PR was a unique high resolution, high efficiency γ-ray imaging device consisting of 64 0.04-X_0 sandwiches made of 8 mm thick scintillators and 6 mm thick cathode-strip drift chambers. The resolutions expected at 500 MeV were 250 μm, $3\%/\sqrt{E(\mathrm{GeV})}$, 25 mrad, and 90 ps/$\sqrt{E(\mathrm{GeV})}$ for position, energy, angle (at 250 MeV), and time, respectively, based on prototype measurements and simulations. Efficiency of detection for photons in the PR which was 2.7 X_0 thick was expected to be 88%.

During the past year, the work was aimed at development of full size elements of the PR system including 1.5×1.5 m^2 chambers and 1.8×1.8 m^2 planes of scintillator, in addition to continuing studies of basic characteristics with prototypes.

The original chamber design employed commercially produced cathode-strip foils that required considerable labour for precision lamination on to large FR4 plates. A procedure of machining copper/FR4 laminations to form copper strips on an FR4 sheet using a high precision router was developed. Tests proved that the router machining produced a very clean copper edge on FR4. Since large size planes of FR4 (or G10) were not commercially available, we started development of such sheets with a local company, Profile Composites Inc. (Sidney, BC). After several iterations, 1.7×1.7 m^2 FR4 sheets with laminated Cu foil were produced with satisfactory quality.

During the past three years we also perfected the production of low-cost extruded polystyrene scintillator in cooperation with another local company, CELCO Industries (Surrey, BC). The polystyrene extrusion chemistry and technique were modelled after work done at Fermilab which produced small cross section single hole scintillators. The extrusion planks we made have dimensions 0.8 cm × 7 cm × 250 cm with six 1.2 mm holes separated by 1 cm for wave length shifting (WLS) fibres. We developed the techniques to reliably extrude multiple hole planks with uniform dimension holes, and achieved reasonable dimensional tolerances of <0.15 mm for flatness and <0.4 mm for excursions from "straightness" over 2 m lengths. Following a production run of about 500 planks at CELCO (May, 2005), we established the procedures to glue scintillator planks together (with the edges machined to a tongue-and-groove shape) using a specially prepared glueing jig. Figure 7 shows glueing in progress on the jig.

We have studied basic properties of scintillators and the readout scheme with 1 mm diameter WLS fibres. The tests indicated that the amount of the scintillation light in the produced extruded scintillator was comparable to that of the commercial cast scintillator BC408. Light attenuation in the extruded material including surface effects was found to be shorter (20–30 cm) than in BC408; this feature was of minor

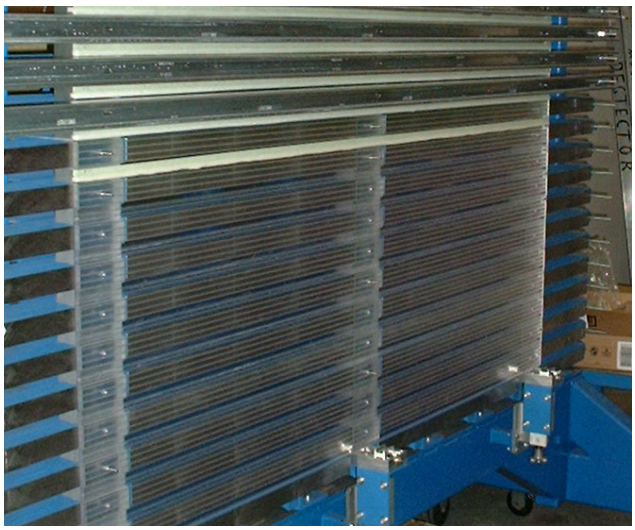

Fig. 7. Fabrication of scintillator plane. Eleven planks in the lower section have been glued.

importance in the WLS readout geometry studied. It was also established that there was little variation of the light yield (1.5%) across the scintillator planks and across the joints when the scintillators were glued together with optical cement. In addition, it was found that the quality (surface imperfections and diameter variations) of the extruded holes had little effect on the light output. The measured time resolution for the single end readout was found to be $\Delta t = 90$ ps$/\sqrt{E(\mathrm{GeV})}$ with a 700 ps constant term.

We also studied different wrapping materials and coatings. Using a small piece of extruded scintillator (40 cm long) with a 1.4 m WLS fibre we tested commonly used and unconventional materials, and observed a significant improvement in the light yield with two of them, 3M enhanced specular reflector (ESR) and Avian-D paint. Results are shown in Table I. The tests also indicated that even one layer of paint (0.11 mm thick) would provide sufficient light output (88% of the maximum) and with two layers of paint (0.28 mm thick) one would see saturated light output. These results would correspond to energy resolution of $\sigma_E < 1\%/\sqrt{E(\mathrm{GeV})}$ from photon statistics.

The KOPIO readout electronics hardware can be separated into three main components: anode readout (TDC), cathode readout (ADC), and data collector. The anode readout cards consisted of the ASD01 (amplifier, shaper, discriminator), the ATLAS AMT-3 (TDC), and an FPGA. Development of the anode readout was well advanced, with the 96-channel readout card designed and ready for manufacturing. After the cancellation of KOPIO, the design was modified to accommodate more general demands. The 48 channel TDC module provides 0.625 ns timing resolution operating at 50 MHz. The inputs of the module are 48 LVDS pairs, organized in groups of 16 to easily match the output of the preamp cards. Configuration of all TDC parameters occurs through the VME interface. In order to synchronize with other TDC modules in the system, the clock and bunch reset (coarse time count reset) are to be fed in externally.

Table I. Effect of wrapping materials on the single end light yield (p.e./MeV) from the extruded scintillator read out with WLS fibres using cosmic rays. The fibres were blackened on the non-readout end.

Material	p.e./MeV
Black absorber (paper)	3.6
Aluminized mylar	10.4
Plastic-backed Al foil	10.1
Tyvek	9.1
3M enhanced specular reflector	16.4
Avian-D paint	16.2

The cathode readout cards consisted of the CMS Buckeye front end chip, the ADS5271 (serial output ADC), and an FPGA. A version of the readout section (VF48) was completed using a parallel output version of the ADC and is being made for several other projects. The VF48 channel ADC module uses 10 bit parallel output ADCs at 40 MS/s (ADS5120). It should also be possible to run this card using 10 bit 65 MS/s ADCs (ADS5122). Much of the design work for the TDC module overlaps with the anode readout from the KOPIO experiment. Prototypes were also designed and tested for the preamps.

Besides the development of the hardware, firmware was needed. Various aspects of the firmware were developed including control for the front-end electronics, ASD01 and Buckeye, control for the AMT-3 TDC, and the VME interface.

The HERMES Experiment

(C.A. Miller, S. Yen, TRIUMF)

Introduction

The HERMES experiment was designed to comprehensively study the spin structure of the nucleon. It has been running at the 27.5 GeV HERA electron accelerator at the DESY Laboratory in Hamburg, Germany since 1995, measuring spin asymmetries for deeply inelastic electron scattering (DIS) as well as a wealth of unpolarized observables. The combination of a polarized high energy electron beam in a storage ring with undiluted polarized atomic gas targets is unique in this field, and has important experimental advantages. Furthermore, the spectrometer detecting the scattered electrons has substantial acceptance and the capability to identify all types of hadrons produced in coincidence. The Canadian group led by TRIUMF designed, built and maintains the transition-radiation detector, which is a crucial component for identifying electrons in a large hadronic background.

Since the long HERA shutdown in 2000–2001, HERMES has been running with a transversely polarized hydrogen target, recording the first and only such data thus far for both DIS and hard exclusive processes. The spin physics community had been eagerly anticipating this data, as it gives access to new and crucial types of information about nucleon structure, as described in detail below. HERA's performance in 2005 was greatly improved over recent years, with the result that our total data set with the transverse target polarization was more than doubled. This marks a successful end of this era of the experiment, as the polarized target was removed at the end of 2005 to make way for the new recoil detector system, which will surround a high-luminosity unpolarized target cell for the remainder of HERA operation ending in mid 2007.

New results from the 2005 running period will be released in 2006. Meanwhile, analysis has continued on all of the data accumulated since 1996, especially those recorded recently. Space limitations prevent inclusion here of all the new results released in 2005. Only some highlights are presented.

Helicity density of the strange quark sea

The contribution of strange quarks to the nucleon spin continues to be a subject of controversy. Interpretation of asymmetries measured in inclusive lepton DIS with longitudinally polarized beam and target, incorporating hyperon beta decay data through the assumption of SU(3) flavour symmetry, indicates that the strange sea is significantly negatively polarized. As has been described in previous Annual Reports, a key part of the HERMES spin physics program has focused on the study of semi-inclusive DIS, in which an identified energetic hadron is detected in coincidence with the scattered lepton. As most such hadrons are created in the fragmentation of the struck quark, their identity carries statistical information about the flavour of the quark. This method of flavour-tagging applied to longitudinal double-spin asymmetries was exploited to yield the first measurement of the quark helicity densities for all three light quark flavours including sea quarks (see the 2002 Annual Report). This extraction was based on the model for the fragmentation process that is represented in the JETSET simulation system, tuned for HERMES kinematics. The result suggested that the polarization of the strange sea is small. Now another "isoscalar" approach has been applied to the same data set to extract the net helicity density $\Delta S \equiv \Delta s + \Delta\bar{s}$ of the strange quark sea, while extracting the required fragmentation information from HERMES data. Aside from isospin symmetry between proton and neutron, the only symmetry assumed is charge conjugation invariance in fragmentation.

Because strange quarks carry no isospin, the net helicity densities ΔS in the proton and neutron are identical. In the deuteron, an isoscalar target, the fragmentation process in DIS can be described without any assumptions regarding isospin dependence of the fragmentation. The isoscalar extraction method requires only the inclusive asymmetry $A_{1,d}(x)$ and the asymmetry $A_{1,d}^{K\pm}(x)$ for both charged kaons combined, to determine two unknowns – ΔS and the total non-strange quark helicity density $\Delta Q \equiv \Delta u + \Delta\bar{u} + \Delta d + \Delta\bar{d}$. Here Bjorken-$x$ represents the fraction of the nucleon's "infinite" longitudinal momentum carried by the quark. The inclusive asymmetry is related to the unknowns via the two "composite" parton distribution functions (PDFs) $Q \equiv u + \bar{u} + d + \bar{d}$ and $S \equiv s + \bar{s}$:

$$A_{1,d}(x) = \frac{5\Delta Q(x) + 2\Delta S(x)}{5Q(x) + 2S(x)}.$$

The fragmentation functions $D_q^{K\pm}(z)$ needed to interpret $A_{1,d}^{K\pm}(x)$ are extracted directly at HERMES kinematics from the x dependence of the measured combined multiplicity of charged kaons corrected to 4π acceptance, which is shown in Fig. 8. The fit shown exploits the known x dependence of $Q(x)$ and $S(x)$ to determine two composite fragmentation functions integrated over the range $0.2 < z < 0.8$, where z represents the energy of the detected hadron as a fraction of the energy of the virtual photon (or struck quark):

$$\begin{aligned}\int dz\, \mathcal{D}_Q(z) &\equiv 4\int dz\, D_u^{K\pm}(z) + \int dz\, D_d^{K\pm}(z)\\ \int dz\, \mathcal{D}_S(z) &\equiv \int dz\, D_s^{K\pm}(z) + \int dz\, D_{\bar{s}}^{K\pm}(z)\,.\end{aligned}$$

Using this information about fragmentation, the charged kaon asymmetry is related to the unknowns via

$$A_{1,d}^{K\pm}(x) = \frac{\Delta Q(x)\int dz\, \mathcal{D}_Q(z) + \Delta S(x)\int dz\, \mathcal{D}_S(z)}{Q(x)\int dz\, \mathcal{D}_Q(z) + S(x)\int dz\, \mathcal{D}_S(z)}\,.$$

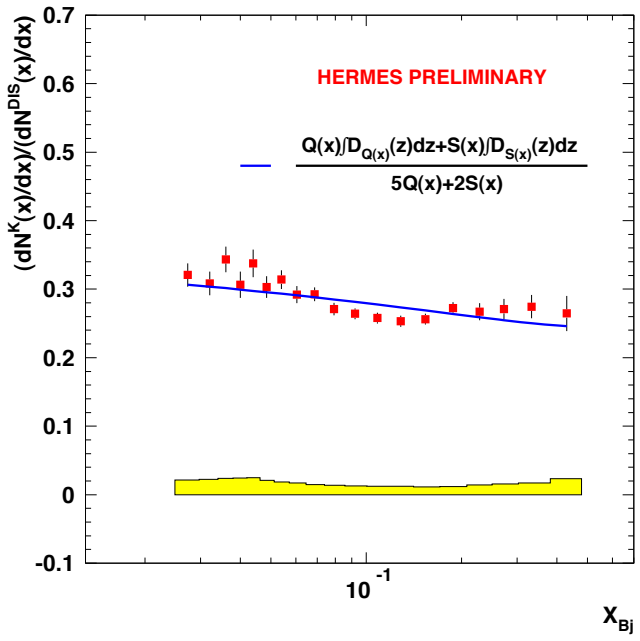

Fig. 8. Multiplicity corrected to 4π acceptance of charged kaons in semi-inclusive DIS off the deuterium target as a function of Bjorken-x. The curve is the fit to the data of the equation indicated in the figure obtained by varying the composite fragmentation functions $\int dz\, \mathcal{D}_Q(z)$ and $\int dz\, \mathcal{D}_S(z)$ integrated over the range $0.2 < z < 0.8$. The error bars are statistical, and the band at the bottom represents the systematic uncertainty.

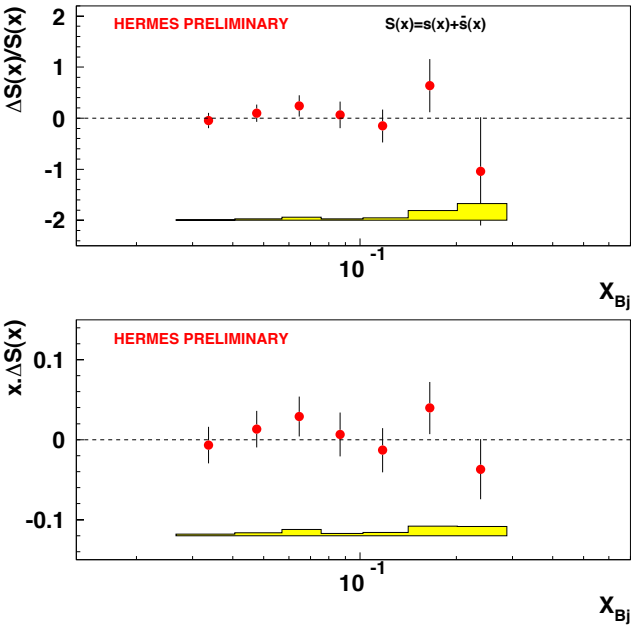

Fig. 9. Strange $(s + \bar{s})$ quark polarization and helicity distribution at $\langle Q^2 \rangle = 2.5$ GeV^2, as a function of Bjorken-x. The error bars are statistical, and the bands at the bottom represent the systematic uncertainties.

The results for $\Delta S(x)$ are shown in Fig. 9. The first moment over the measured range $0.02 < x < 0.6$ is found to be $\Delta S = 0.006 \pm 0.029 \pm 0.007$. This magnitude is substantially smaller than the significantly negative values that are derived from only inclusive scattering under the assumption of SU(3) flavour symmetry in the interpretation of hyperon beta decay. Hence this result suggests that the strange sea makes little contribution to the nucleon spin.

Single-spin asymmetries in semi-inclusive DIS

As was first demonstrated by HERMES, single-spin asymmetries can appear in semi-inclusive DIS when the spin observable involves either a parton distribution function or a fragmentation function that is "T-odd". An amplitude is (naively) T-odd when it is invariant under inversion of the sign of all momenta and angular momenta *without* interchange of the indices indicating initial and final states. As was explained in more detail in the 2003 Annual Report, asymmetries involving only transverse target polarization are sensitive to two very different aspects of nucleon structure. One is *transversity*, the last to be measured of the three basic twist-2 parton distribution functions describing the nucleon. It represents the number density of transversely polarized quarks in a nucleon polarized transversely with respect to its "infinite" momentum. Transversity can differ from helicity densities in a relativistic bound state, as boosts and rotations do not commute in a relativistic context. Transversity can give rise to an observable asymmetry through the action of a T-odd fragmentation function called the Collins function, which acts as a "polarimeter" for transverse quark polarization.

The other new aspect of nucleon structure that can create asymmetries with respect to only transverse target polarization is a T-odd distribution function called the Sivers function, which describes the correlation between the direction of the nucleon spin and the intrinsic transverse momentum of the quark. Recent theoretical advances have revealed deep connections between the Sivers function and the contribution of each quark flavour to the anomalous magnetic moment of the nucleon, as well as to the orbital angular momentum of the quarks [Burkardt, Phys. Rev. **D72**, 094020 (2005)]. Furthermore, it was realized only a few years ago that QCD predicts that the Sivers function as measured in the Drell-Yan process should have the opposite sign (but the same magnitude) as observed in DIS of leptons [Collins, Phys. Lett. **B536**, 43 (2002)]. This prediction will be important to confirm.

As explained in the 2002 Annual Report, the Collins and Sivers effects can be disentangled through their different dependence on the azimuthal angles of the detected hadron about the direction of the exchanged virtual photon, with respect to the lepton scattering plane and the plane of the target polarization (see Fig. 10). That report showed the first results from the 2002–2003 data set, which provided evidence for substantial magnitudes of both Collins and Sivers asymmetries. A surprising feature of the Collins asymmetry for π^- mesons was that it appeared to be opposite in sign and at least as large in magnitude as for π^+.

The 2004 data set is almost twice as large as that of 2002–2003. New preliminary results from 2002–2004 are shown in Figs. 11 and 12, as a function of Bjorken-x, z, and $P_{h\perp}$ representing the momentum component of the hadron perpendicular to the direction of the virtual photon. The new data clearly confirm the indications of the earlier data. Furthermore, additional investigations have laid to rest concerns that these

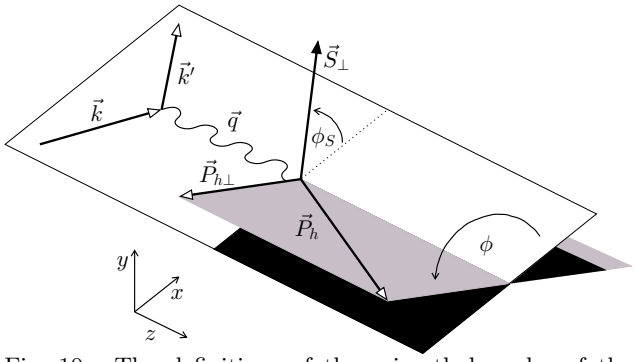

Fig. 10. The definitions of the azimuthal angles of the hadron production plane and the target spin axis.

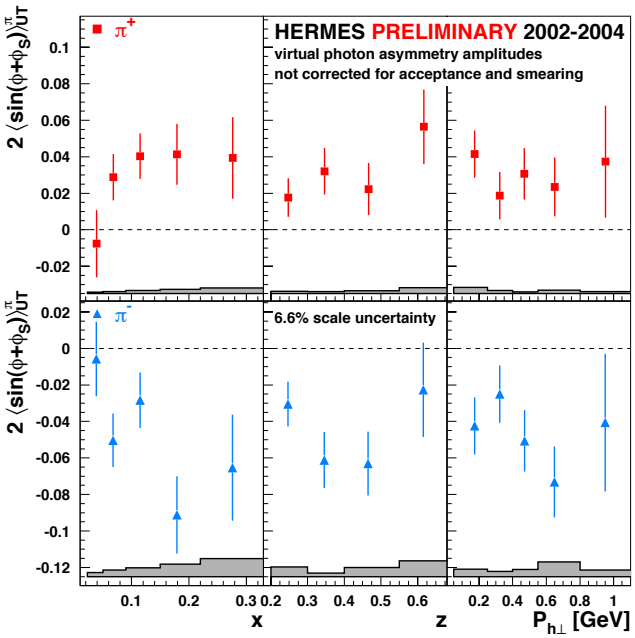

Fig. 11. Collins asymmetries for electroproduction of charged pions as labelled, as a function of three kinematic variables defined in the text. The error bars represent the statistical uncertainties, while the lower band represents the systematic uncertainty. In addition, there is a common overall scale uncertainty that is 6.6% of the central value in each bin.

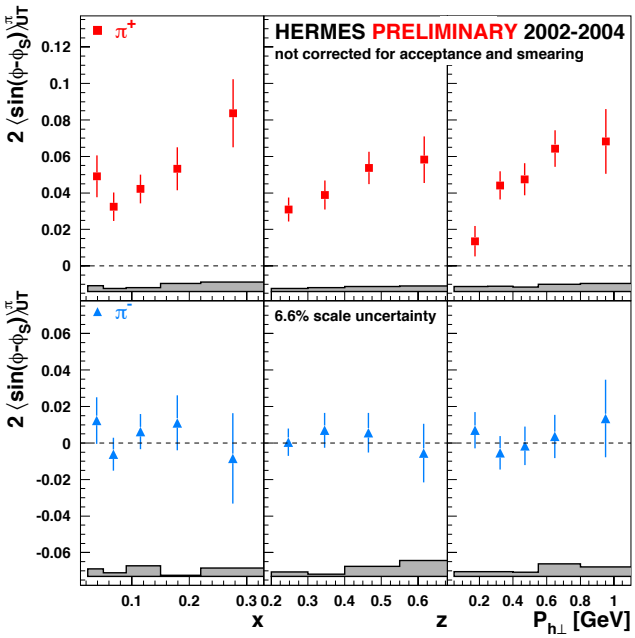

Fig. 12. Sivers asymmetries for electroproduction of charged pions as labelled. The uncertainties are shown as in Fig. 11.

asymmetries could be largely the result of contributions from the decay of exclusively produced vector mesons, which can be significant especially at large values of z. The improved statistics allowed the asymmetries to be fitted in multiple kinematic dimensions using the maximum likelihood technique, resulting in consistency with zero of the coefficient of $-Q^2$, which is the square of the four-momentum of the virtual photon. The contributions of exclusive processes would be suppressed by powers of $1/Q$. Furthermore, asymmetries formed from differences in yields of π^+ and π^-, in which the contributions of exclusive processes cancel, were also found to be substantial. Hence the new data provide the first firm evidence of a T-odd distribution function in leptoproduction, as well as a substantial value for the Collins fragmentation function, which will give the first access to the previously unmeasured transversity distribution.

Quantitative interpretation of the Collins asymmetries in terms of transversity will be based on values of the Collins function now being extracted from high-statistics e^+e^- data recorded by the Belle Experiment at KEK. However, these asymmetries have already been found to be in good agreement with predictions of transversity based on the chiral quark soliton model in combination with an estimate of the "favoured" Collins function based on DELPHI data, and a surprisingly large ratio of disfavoured to favoured Collins functions of -1.2 [Efremov *et al.*, Czech. J. Phys. **55**, A189 (2005)]. A (dis)favoured fragmentation function describes fragmentation of a quark into a hadron (not) containing a valence quark of that flavour.

As the Sivers asymmetry involves the well-known conventional unpolarized fragmentation functions, values of the Sivers distribution function can be extracted from the asymmetries using the same type of analysis that was used to extract helicity distributions from longitudinal double-spin asymmetries. Such a preliminary analysis reveals that the Sivers function for *up* quarks is strongly negative in value over the entire measured x range, while for *down* quarks, it is less well defined, depending on assumptions made for the sea quarks. No model yet gives a good description of all of these Sivers asymmetries.

Single-spin asymmetries in di-pion production

The Collins function is not the only T-odd fragmentation function that can provide experimental sensitivity to transversity. Almost a decade ago, it was theoretically predicted [Jaffe *et al.*, Phys. Rev. Lett. **80**, 1166 (1998)] that in production of a hadron consisting of a $\pi^+\pi^-$ pair, interference between the s and p states of relative orbital angular momentum of the pair could give rise to the non-trivial phase that is necessary for T-odd character. If the fragmentation function describing the resulting sensitivity to the transverse polarization of the struck quark (called an *interference* fragmentation function in some of the literature) were found to have a substantial magnitude, it would provide an alternative way to measure transversity. It

would be free of a complication of the factorization theorem that arises in connection with the Collins function due to the central role played in that case by transverse parton momenta involved in the fragmentation process.

The 2004 Annual Report mentioned that a single-spin asymmetry involving longitudinal target polarization offered the first evidence that the above-described T-odd dipion fragmentation function is substantial. Since then, the relevant $\pi^+\pi^-$ azimuthal asymmetry has been extracted from the 2002–2004 data set with transverse target polarization. In this case, a particular Fourier component of the angular dependence is uniquely related to a combination of transversity with the T-odd fragmentation function. The relevant angles are defined in Fig. 13, and the extracted asymmetries

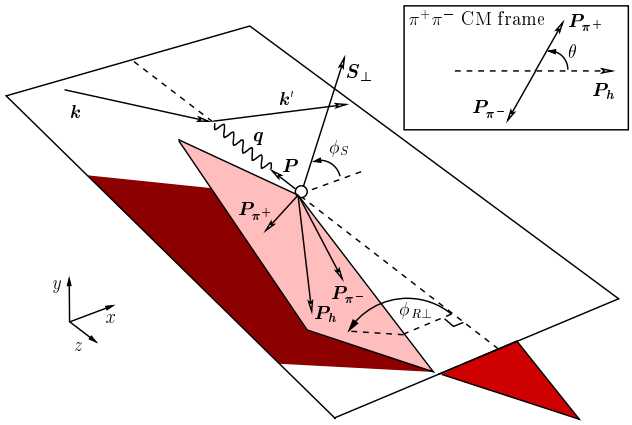

Fig. 13. Definition of kinematic variables for semi-inclusive production of $\pi^+\pi^-$ pairs in DIS.

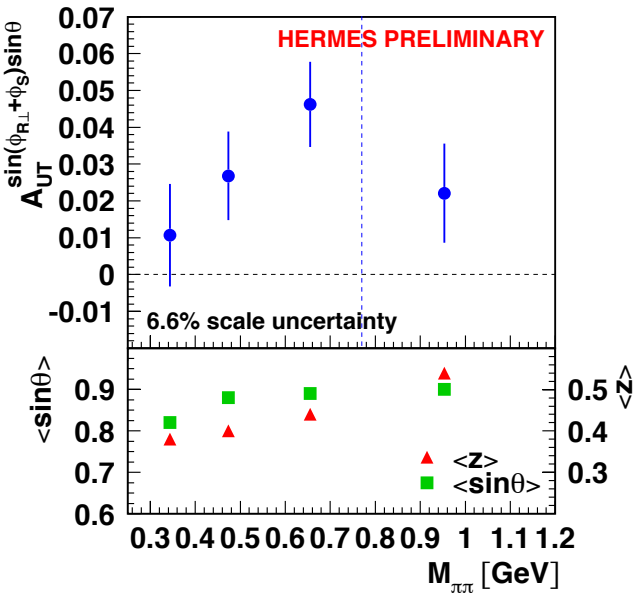

Fig. 14. The amplitude of the indicated Fourier component of the asymmetry with respect to transverse hydrogen target polarization, as a function of the invariant mass of the $\pi^+\pi^-$ pair detected in semi-inclusive DIS. The lower panel shows the average $\langle \sin\theta \rangle$ and the average z for each invariant mass bin.

are shown in Fig. 14 as a function of the invariant mass of the system of two pions.

The observed asymmetry has a large statistical significance, and shows no indication of the change in sign at the ρ^0 mass that was predicted in one theoretical model. Efforts are under way to extract the relevant T-odd fragmentation function from e^+e^- data recorded by the Belle Experiment. When this is accomplished, this asymmetry signal will provide another independent constraint on transversity.

Quark total angular momentum J_q from deeply virtual Compton scattering

As a result of remarkable theoretical advances over the last decade in the understanding of the investigation of QCD bound states via lepton scattering, elastic form factors and parton distribution functions are now integrated into the unified framework of generalized parton distributions (GPDs). Hard exclusive reactions that involve several hard vertices yet finally leave the target nucleon intact have been found to provide experimental access to the dependence of GPDs on their three kinematic variables: Mandelstam t representing the four-momentum transfer to the target, and the combinations $x+\xi$ and $x-\xi$ representing the longitudinal momentum fraction of the quark before and after the process, respectively. The "skewness" ξ is related to $x_{Bj} = Q^2/(2M\nu)$ via $\xi \simeq x_{Bj}/(2-x_{Bj})$, where M is the target mass and ν is the energy of the virtual photon in the target rest frame. (This role of x_{Bj} differs from that of Bjorken-x in the case of DIS.) On the other hand, x may be a hidden variable in DVCS, as some observables appear as x-convolutions of GPDs with hard-scattering kernels.

One feature of GPDs that has attracted a great deal of attention is that, if they can be sufficiently constrained by measurements of various observables for several hard exclusive reactions, it should be possible for the first time to determine the net contribution $J^q = S_q + L_q$ of quark *total* angular momenta to the nucleon spin via the now-famous Ji relation [Ji, Phys. Rev. Lett. **78**, 610 (1997)]:

$$J^q = \lim_{t\to 0} \frac{1}{2} \int_{-1}^{1} dx\; x\,[H^q(x,\xi,t) + E^q(x,\xi,t)]\,.$$

Here the function H (E) is the so-called unpolarized (spin-flip) GPD, which is related to the Dirac (Pauli) elastic form factor:

$$\int_{-1}^{1} dx\; H^q(x,\xi,t) = F_1^q(t)$$
$$\int_{-1}^{1} dx\; E^q(x,\xi,t) = F_2^q(t)\,.$$

In the forward limit of vanishing momentum difference between the initial and final hadronic state ($t \to 0$ and $\xi \to 0$), the GPD $H^q(x,0,0)$ reduces to the quark number density distribution $q(x)$.

Deeply virtual Compton scattering (DVCS), the production of only an energetic real photon by a hard virtual photon, is considered to be the most interpretable of the hard exclusive processes, as NLO QCD corrections and those for higher twist are already under theoretical control. Furthermore, the DVCS process has the unique virtue that it interferes with the well understood Bethe-Heitler process of radiative elastic scattering from the nucleon target, fortuitously giving rise to a rich variety of large asymmetries in either beam or target polarization or beam charge, appearing in the azimuthal distribution of detected photons about the direction of the virtual photon. This interference provides access to the DVCS scattering *amplitudes*.

As shown in the 2002 Annual Report, the first observation of a DVCS beam spin asymmetry was reported by HERMES in 2000, followed by a beam charge asymmetry in 2002. Now HERMES has accumulated a substantial 2002–2005 data set with *transverse* hydrogen target polarization, which provides unique sensitivity to the otherwise-elusive GPD E. Preliminary results have been extracted from the 2002–2004 data for particular Fourier harmonics of the dependence of the transverse target polarization asymmetry on the azimuthal angles of the detected energetic photon about the direction of the virtual photon with respect to both the lepton scattering plane and the target polarization direction (see Fig. 10, where here P_h becomes the momentum of the energetic real photon).

Figure 15 shows two particular azimuthal Fourier amplitudes of the azimuthal dependence of the DVCS asymmetry that are uniquely sensitive to the GPDs H and E. They are compared to theoretical predictions based on the GPD model of Goeke, Polyakov and Vanderhaeghen [Prog. Part. Nucl. Phys. **47**, 401 (2001)], using three different values of J_u, the total angular momentum of *up* quarks in the proton, while $J_d = 0$. The present data set has useful sensitivity to J_u, while it has been found that these predictions of this model are remarkably insensitive to other model parameters [Ellinghaus *et al.*, hep-ph/0506264]. Addition of the 2005 data set will improve this first direct experimental constraint on the total angular momentum of quarks.

Outlook

HERA will operate until mid-2007. At the end of 2005, HERMES installed a new recoil detector to surround the target cell and detect the recoiling intact target nucleon from hard exclusive processes, in order to guarantee their exclusivity. This detector will

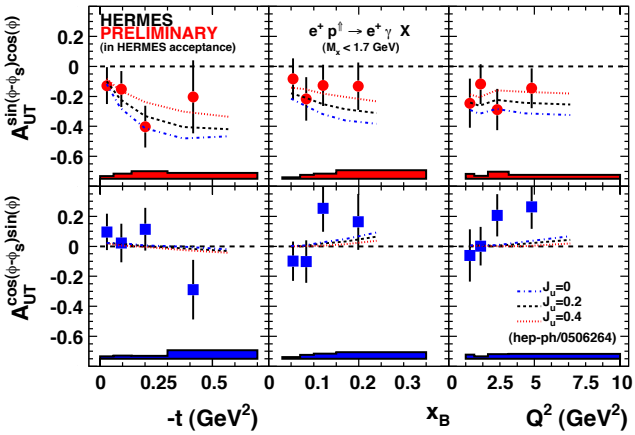

Fig. 15. The indicated azimuthal Fourier amplitudes of the asymmetry with respect to tranverse polarization of a hydrogen target for the cross section of deeply virtual Compton scattering, plotted as a function of the three indicated kinematic variables. The curves are predictions based on a model for the generalized parton distributions H and E, using three different values of J_u, the total angular momentum of *up* quarks in the proton, while $J_d = 0$.

be the centre-piece for the remainder of HERMES operation, using high density unpolarized targets. This will yield the first really high quality data on asymmetries in both beam spin and charge for DVCS, the process that holds the most promise to shed light on the total angular momentum of partons.

HERMES collaborators in 2005: C.A. Miller, S. Yen, TRIUMF; G. Gavrilov, TRIUMF/DESY.

J-PARC

T2K long baseline neutrino experiment

(A. Konaka, TRIUMF)

Introduction

The goal of the T2K (Tokai-to-Kamioka) long baseline neutrino oscillation experiment is to measure the neutrino oscillation parameters precisely, in particular to observe the ν_μ to ν_e oscillation through the mixing angle θ_{13} for the first time. Neutrino oscillation probability (P) is described as $\mathrm{P} = \sin^2 2\theta \sin^2 \frac{1.27\Delta m^2 L}{E}$ where θ is the mixing angle, L is the distance, and E is the neutrino energy. By comparing the neutrino energy spectra between near and far detectors, one can study the neutrino oscillation parameters in detail.

The neutrino source of the T2K project is the J-PARC proton accelerator, which is under construction in Tokai, Japan. It is going to be the first MW class machine in the proton energy range of 30–50 GeV. The proton beam hits a graphite target and produces pions, which are then focused by three stages of horn magnets in the direction of the Super-Kamiokande (SK) detector 295 km away. The pions decay $\pi \to \mu\nu_m u$ in the decay pipe to produce neutrinos whose flux and energy spectrum are monitored by the detector at 280 m

(ND280) downstream of the target. The direction of the neutrino beam is actually set 2–3° away from the SK direction to provide a narrow band neutrino energy tuned at the oscillation maximum (off-axis beam). Commissioning of the accelerator is expected in May, 2008, and commissioning of the neutrino beam is scheduled in April, 2009.

Since the accident in 2001, the SK detector has been operating with half of the PMTs. During 2005, the reconstruction of the SK detector took place. The Canadian T2K group contributed to the reconstruction shifts. Figure 16 shows a picture taken by a co-op student from Canada during the reconstruction work.

TRIUMF scientists have been involved in the J-PARC accelerator and T2K neutrino beam line designs. Ewart Blackmore (Chair) and Clive Mark from TRIUMF served on the neutrino technical advisory committee in April. In the spring, TRIUMF's Five-Year Plan budget, including external accelerator contribution, was approved. In June, T2K beam line representatives from KEK visited TRIUMF. Contributions to remote handling for the final focusing monitor, hot cell, and the optical transition radiation (OTR) beam monitor right in front of the target were requested, and a collaboration on the design work started.

The Canadian T2K group was awarded an NSERC grant to develop a near detector design in 2005. In August, the T2K near detector (ND280) collaboration meeting was held at TRIUMF. About 60 people attended the meeting from Japan, Europe and North America. At the meeting, the near detector conceptual design report was prepared and discussed. The Canadian T2K group took the responsibility of the tracker, which consists of two fine grained detectors (FGD) and three time projection chambers (TPC). In September a 3 year grant request was submitted to NSERC to construct the FGD, TPC and OTR. By the end of the year, prototypes of these three detectors were constructed and tested with the beam and cosmic rays. Details of the detector components and the prototype results are described in the following sections. The photosensor for the FGD is provided by the Japanese and Russian groups, and the TPC electronics is provided by the French group. Spanish and Swiss groups also participated in the TPC project. The European groups contributed a UA1 magnet as a spectrometer, the UK group contributed the electromagnetic calorimeter, and the US group contributed to a detector designed to detect π^0s. The Canadian group also takes part in the integration of the ND280 detector, and has two representatives (Roy Langstaff and Chris Hearty) on the ND280 technical board. Canada is also responsible for maintaining the document and communication Web server for the whole ND280 collaboration (www.nd280.org), which is physically located at TRIUMF.

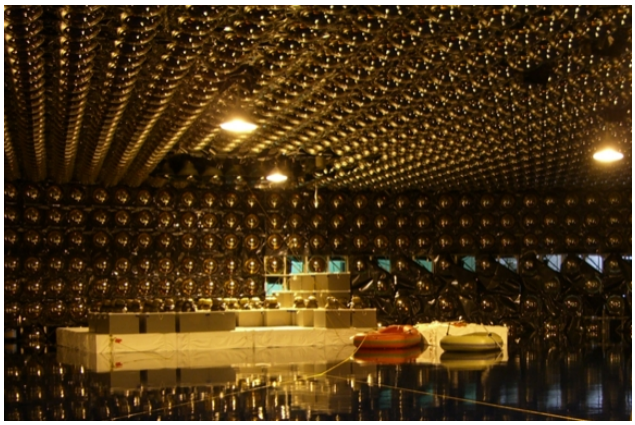

Fig. 16. SK reconstruction work.

Accelerator and beam line

J-PARC accelerator and the neutrino beam line construction are proceeding on schedule. Commissioning of the main ring is expected in May, 2008 and the fast extraction of the beam to the neutrino target is scheduled in April, 2009. Figure 17 shows various scenarios for intensity upgrades after commissioning.

The beam intensity of the first year is expected to be 1–10% of the first phase goal of 0.75 MW and to ramp up rapidly. TRIUMF accelerator physicists have been involved in the beam dynamics study of J-PARC, and asked to contribute to the study of beam instability and to construct the transverse beam damper in the main ring. These are critical in the ramp up of the beam intensity. This contribution is part of the external contribution in the TRIUMF Five-Year Plan. After a few years of operation, the 400 MeV linac will be upgraded and a flywheel added for the rf power supply, which will further increase the intensity by increasing the number of protons in each bunch and the repetition rate of the acceleration cycle. The beam intensity is expected

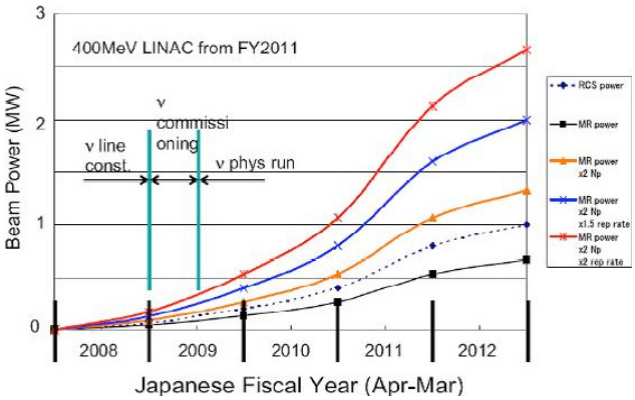

Fig. 17. Scenarios for J-PARC beam power upgrades. The orange line in the middle is considered to be the most likely scenario.

eventually to reach 3–4 MW, getting ready for the second phase of the T2K project for CP violation measurement in the lepton sector.

Handling of the MW scale beam is one of the major challenges in the neutrino beam line. The TRIUMF Remote Handling group has been giving advice for the design of the target station where the MW beam hits the target. The target station components, the beam monitors, window, collimator, target and horns hang from the top below the shielding blocks. The arrangement is very similar to that of the ISAC target station at TRIUMF. TRIUMF is asked to take part in the OTR beam profile monitor in front of the target, the remote handling of the final focusing (FF monitor) beam monitor right upstream of the target station, and the hot cell with manipulator for the remote maintenance of the components in the target station. Figure 18 shows a conceptual design of the support structure of the FF monitor proposed by the TRIUMF Remote Handling group. The design is based on a "smoke stack" design, which is successfully operated in the meson hall.

In the smoke stack, the vacuum extends in the vertical direction by a few metres to a lower radiation area where it is sealed. Inside the smoke stack, there is a shielding iron block below which the beam profile and position monitors hang. The beam line components, including the smoke stack and the OTR monitor, are scheduled to be installed in the fall of 2008.

Optical transition radiation detector

The Canadian group has proposed and been assigned responsibility to build an optical transition radiation (OTR) detector immediately in front of the production target. An OTR device is the only technology that can be placed in the intense beam and survive while neither disturbing the beam emittance nor producing significant radiation.

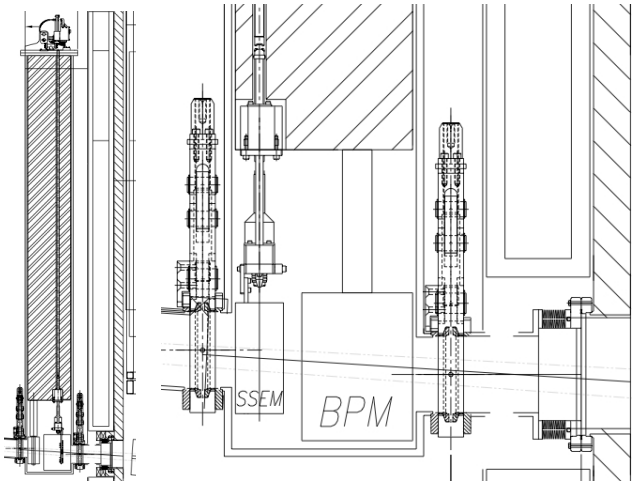

Fig. 18. The remote handling design of the final focusing monitor. The left figure shows the smoke stack vacuum pipe. The vacuum box which contains beam position and profile monitors is attached at the bottom of the smoke stack. The right figure shows a magnified view of the vacuum box.

OTR light is emitted at the boundary between two materials with different dielectric constants, and can be detected by a camera. The light is emitted in forward and backward cones. We will use the backward cone, which reflects at 90° to the beam if the foil is placed at a 45° angle – the amount of light produced is more than ample.

OTR monitors have been used in electron and proton machines, for example in a 26 GeV proton beam at CERN and a 120 GeV proton beam at Fermilab. Because OTR is a boundary effect, the target foil can be extremely thin. The OTR detector at Fermilab has been operated successfully in air. In our case, the monitor will operate in helium gas at atmospheric pressure, since helium is used to cool the target station.

Thermal stress and radiation damage We have used the MARS simulation program to study temperature and mechanical stress effects in the OTR foil. We simulated the distribution of energy deposited in the foil by the proton beam to determine the resulting temperature rise and induced thermal stress. For a number of foil materials the thermal stress induced is less than the allowable stress, defined to be one third the tensile strength of the material. The stress does not depend on the foil thickness, since the energy deposition is uniform through the thickness. Our calculations indicate that shear stress is unimportant. Hence thermal stress does not appear to be a problem. We have also done further stress calculations and, in particular, transient stress, and we are consulting experts at TRIUMF and FNAL.

The beam heats the OTR foil until it reaches a steady-state temperature or it melts. We simulated the steady-state temperature of the OTR foil, taking into account convective, radiative and conductive cooling in the target station's helium gas environment, as well as radiative heating due to the foil's proximity to the T2K production target. The maximum steady-state temperature was found to occur when the proton beam width was 3.5 mm, this being the smallest beam size expected for the T2K beam. The melting points of all the materials investigated are above 1500°K, much greater than the calculated steady-state temperatures.

Radiation damage is a concern due to the high T2K intensity, where we expect 10^{21} protons on a 6 mm$^{\phi}$ spot each year. This year we are preparing to test foils at a TRIUMF target station in a helium environment in order to study radiation and reflectivity effects.

The OTR optical system Figure 19 is a schematic diagram showing the various components that are

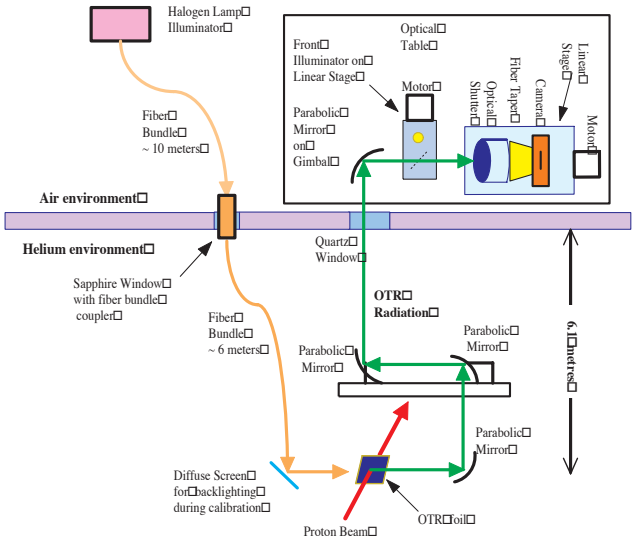

Fig. 19. OTR system design.

loosely called the OTR system. A radiation hard optical window at the helium lid allows light to travel to mirror 4, which is outside the helium vessel. The dogleg shape of the optical system is to prevent direct shine of radiation from the target area reaching the lid of the helium vessel. Mirror 4 projects light onto the image plane of the imaging assembly. The foil assembly is situated on a ladder and moved with an actuator. The image capture system will be placed on an optical table. We envisage a system for back lighting the foil for calibration purposes.

OTR foils will be made of 10–50 μ thick Ti alloy or graphite and stretched individually on their own frames, and assembled in the form of a ladder on a holder, as shown in Fig. 20. Multiple foils will allow for longer periods between service in case of foil breakdown. One reference foil will occasionally be exposed to the beam to monitor the degradation of the surface reflectivity of the main foils due to extended exposure to the proton beam. The foil ladder will be controlled by an actuator which will support, align and position OTR foils with respect to the proton beam. The design of the actuator and alignment systems is currently a central activity of a Toronto engineer.

Our design has evolved considerably through many iterations. The primary optical program we use is OSLO. Most of the ray-tracing and illumination distributions are produced with programs written by York University students in C++, which have been cross-checked with OSLO. The criteria we use to assess each design in the observation of the OTR peak are the uniformity of response across the aperture, and the blurriness and distortion of the image.

The design of the T2K OTR optics system is complicated by the fact that the light must be brought out by an arrangement of mirrors in narrow channels

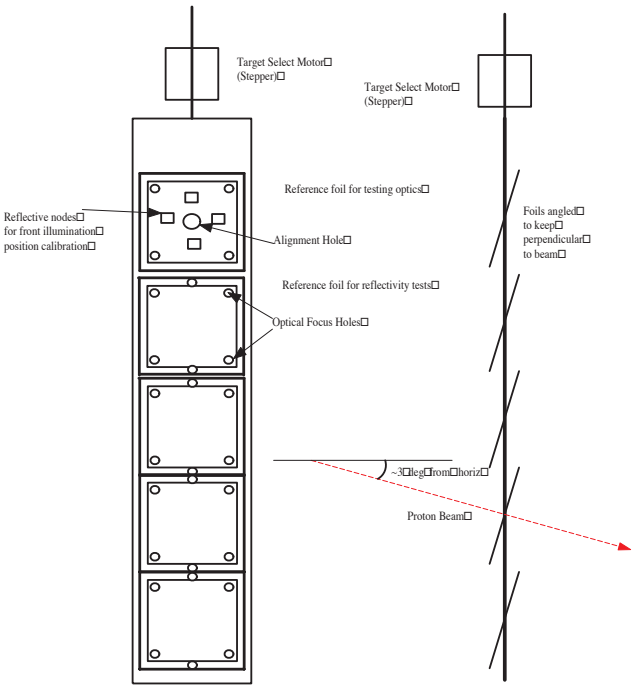

Target Ladder with Alignment Holes

Fig. 20. Target ladder.

through the shielding (a distance of many metres) in order to be observed and read out by a digital camera system. The optics have to include 90° bends in order to eliminate direct paths for radiation leakage. Considerable care must be taken with the mechanical engineering in order to preserve alignment and make allowance for calibration systems. We are working in close collaboration with J-PARC and KEK physicists and engineers, and had a meeting at TRIUMF in January and April to accelerate convergence to the final design parameters and constraints. It has been decided to mount the optics system onto the target support box for mechanical stability and to guarantee the relative alignment between the target and optics.

Imaging assembly and DAQ The spill is composed of several (9 or 16) 60 ns bunches, spaced several hundred ns apart. We plan to image individual bunches using a micro channel plate (MCP) as a fast shutter. The MCP is optically coupled via a fibre taper to a camera, which records the light produced by the MCP. By sequencing the camera and MCP, one or more bunches of a spill can be used to create an image of the beam profile. The front face of the MCP is placed at the focal point of the last parabolic mirror. A custom built circuit board will determine which bunches to image, monitor the system timing to prepare for the spill, and control the MCP shutter and the camera and read out video camera after the spill is complete. A target protect signal can be generated by the output register if

the beam position and shape are not within tolerances. The processor will control all the modules in the system, perform image reconstruction, analysis, and target protection tasks. The image data will be shipped to the main data acquisition system after each spill for logging purposes. A TRIUMF systems designer has been in charge of this project.

Prototype tests At York University, we have tested the optics by mounting a scaled-down prototype (15% of the final system) on an optical table and using diffuse light as a source to test the optics. We have compared the resulting images to ray-tracing simulations in order to understand distortions and the uniformity of the response from different regions of the foil. The system is able to produce good images. The simulations and the image show the same distortions and blurring, and hence we have confidence in the design concept and our simulation programs.

The next step is to test the prototype system at the electron linear accelerator at NRC in Ottawa with OTR light. The electron beam energy of up to 20–30 MeV is a perfect match to the J-PARC proton beam of 50 GeV in terms of the Lorentz factor γ. At this time we will also test different foil materials, enclosing them in a helium environment. In June, 2006, the OTR group from TRIUMF, York and Toronto will test this system. An intense period of design of the hardware and DAQ lies ahead.

Tracker

T2K's ND280 detector (see Fig. 21) is a fine resolution magnetized detector designed to measure the neutrino beam's energy spectrum, flux, flavour content, and interaction cross sections before the neutrino beam has a chance to oscillate. These measurements are crucial for predicting the neutrino event distributions at Super-K to which the observed data will be compared in the oscillation analysis. The ND280 sits off-axis in the neutrino beam along a line between the average pion decay point in the decay volume and the Super-Kamiokande detector, at a distance of 280 m from the hadron production target.

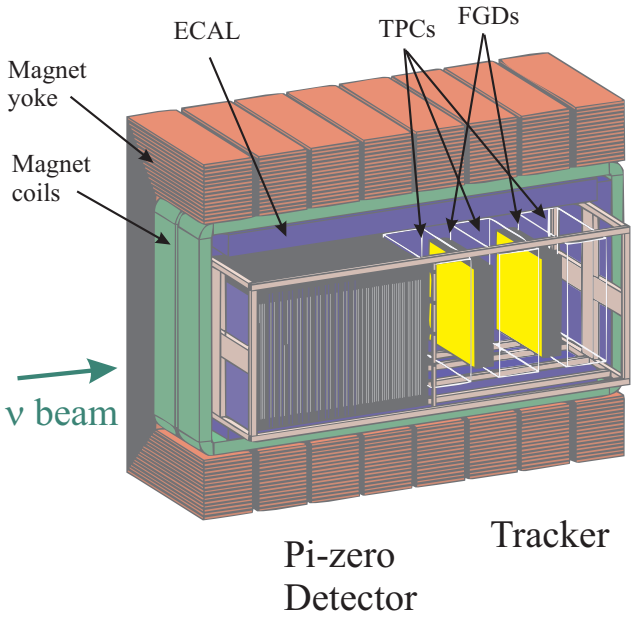

Fig. 21. The T2K ND280 detector.

The Canadian T2K group has been charged with developing the ND280 tracker, which lies at the heart of the ND280. Its primary function is to measure the neutrino flux, energy spectrum, and flavour composition by observing charged current neutrino interactions. Especially important is the CCQE interaction $\nu_\ell + n \rightarrow \ell + p$, which is the most common interaction at T2K's beam energy. For these interactions, the energy of the incident neutrino is calculable from only the energy and direction of the final lepton, with an accuracy limited by the Fermi momentum of the neutron in the nucleus. The tracker must also measure other interactions, particularly those with charged pions in the final state.

To accomplish these goals, the tracker consists of two fine grained detectors (FGDs), sandwiched between three time projection chambers (TPCs). The FGDs provide the target mass for neutrino interactions in the tracker, and measure the direction and ranges of recoil protons and charged pions produced by charged current (CC) interactions in the FGDs, giving clean identification of CC QE and CC non-QE interactions. The three TPCs measure the 3-momenta of muons and other penetrating particles produced by charged current interactions in the detector, and provide the most accurate measurement of the neutrino energy spectrum. The 3D tracking and dE/dx measurements in the TPC also determine the sign of charged particles and identify muons, pions, and electrons.

Fine grained detectors The bulk of the target mass for the ND280 will consist of layers of segmented scintillator bars read out by wavelength shifting fibres. Fine grained segmentation allows tracking of all charged particles arising from neutrino interactions with the target nuclei. In particular, for neutrinos near ~700 MeV, the dominant reaction would be CC-QE: $\nu_\mu\ n \rightarrow \mu^-\ p$, and the ability to track both outgoing particles gives a strong kinematics constraint to reject backgrounds. Using a scintillator, not a Čerenkov detector, allows the detection of particles below the Čerenkov threshold, such as the recoil protons in the above reaction. The scintillator itself provides the target mass for the neutrino interactions. K2K's SciBar detector has demonstrated the utility of such a fine

grained segmented detector, built from extruded plastic scintillator bars.

The ND280 detector will contain two fine grained detectors, each with dimensions of 192 cm × 192 cm × 30 cm (scintillator volume only, not including supports or electronics). One FGD will consist of x-y layers of plastic scintillator bars read out with wavelength shifting fibres, similar to the SciBar detector. The second detector will be a water-rich detector. Initially this detector will consist of x-y layers of plastic scintillator alternating with 3 cm thick layers of passive water.

In the past 12 months, considerable progress has been made in the FGD design. We now possess a finished conceptual design for both the plastic and the passive water FGDs, and are starting on the process of finalizing the detailed design.

Our FGD R&D efforts have concentrated on the following areas:

- Scintillator production: Celco Plastics Ltd. in Surrey, BC originally began R&D production of polystyrene scintillator for the KOPIO experiment. The T2K group has adapted this technology to our particular geometry, and has added co-extrusion of a reflective coating to the procedure. We have recently succeeded in producing 1 cm × 1 cm square bars with a co-extruded TiO_2 coating (see Fig. 22).
- Silicon photomultiplier (SiPM) testing: The FGDs will use silicon photomultipliers to collect light from the wavelength shifting fibres. SiPMs are pixellated photon counters that work like an avalanche photodiode run in Geiger mode. We have carried out an extensive testing procedure for silicon photomultipliers at TRIUMF, using prototype devices supplied by our Russian collaborators. These have included measurements of the relative quantum efficiency of SiPMs compared to conventional photomultiplier tubes and characterization of the noise rates. Members of our group also travelled to Kyoto to collaborate on tests and comparisons with prototype SiPMs produced by the Hamamatsu company.

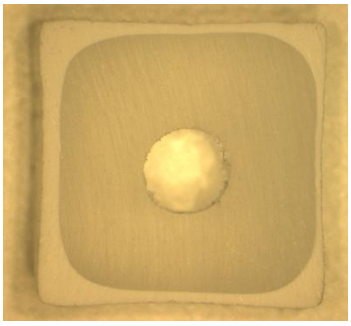

Fig. 22. Cross section of a plastic scintillator bar with co-extruded coating.

- Wavelength shifting fibre studies: We have built a small test stand for measuring the attenuation lengths of wavelength shifting fibres using a movable LED flasher and a photosensor. This set-up has been used to measure the attenuation lengths of different diameter fibres using both SiPMs and conventional photomultiplier tubes.
- Passive water layer construction: We have carried out a series of weight-loading tests in which corrugated plastic sheets have been loaded with sand to the same mass as a passive water layer, and suspended for a period of several months from a crane. These tests confirm the mechanical strength of the water containment for the passive water modules. We have successfully sealed the ends of small corrugated sheets with a thermal weld to a polypropylene endcap to form a leakproof seal that has been successfully tested under pressure. We have also successfully sealed the ends of the panels using epoxy. We are now proceeding with scaling up these sealing processes to the final size.
- Front-end electronics: The Canadian group is preparing a detailed design for the front-end readout electronics of the FGD. Two candidate ASIC chips are under consideration. We have built prototype test boards of a SiPM voltage supply circuit and have done noise measurements of a number of set-ups.
- The baseline design for the ND280 specifies one all-plastic FGD and a second FGD made from alternating layers of plastic scintillator and passive water. This is a robust default option for an oxygen-rich target. However, the ideal water FGD would contain an *active* (instrumented) water target. This is an option that the Canadian group has already invested a lot of effort in, but which still requires further development. We envision that further R&D work may lead to a future proposal to upgrade the passive water FGD to a fully active detector based on a water-soluble scintillator.

  The advantage of an active over passive water target is that there are no dead layers in a fully active detector. We have been exploring a design for a fully active detector based on a water-soluble liquid scintillator contained in square extruded plastic cells. The present method of construction is to use boards of commercial extruded white polypropylene (sold under the brand names Matraplast or Coroplast). The boards come in sheets measuring 1.2 m × 2.4 m, with a cell size of interior dimensions 0.85 cm

× 0.85 cm and wall thickness 0.075 cm, for an exterior cell size of 1.0 cm. (These are the same panels that will be used to construct the passive water modules for the passive water FGD.) The panels are filled with a cocktail consisting of 70% water, 25% commercial liquid scintillator called Quicksafe A (made by Zinsser Analytic), and 5% Triton X-100 surfactant. A 1.5 mm wavelength shifting fibre (Kuraray Y-11) runs down the centre of the cell. We have carried out a number of beam tests to characterize the light yield of this set-up, and are continuing to study its long-term stability, resistance to aging effects, and sensitivity to temperature variations.

TPC To track and measure the momenta of muons and other products of neutrino interactions in the near detector, the T2K collaboration has selected time projection chambers (TPCs) for the baseline design. The Canadian group has mounted a successful R&D program in developing a TPC for the linear collider and, as a result, the group has been assigned the responsibility to lead the effort to build the TPCs for the T2K near detector. The TPC tracker is a very interesting and challenging project and plays a central role in the T2K experiment. It will be the first large scale TPC design to use the readout technology envisaged for a TPC at the International Linear Collider.

The T2K TPC concept developed by the Canadian group has a double box design constructed with composite panels of rohacell and copper clad G10 skins. Both sides of the inner box walls are routed to leave copper strips that are connected to a voltage divider to define a uniform electric field. The surrounding outer box encloses a separate gas envelope that reduces contamination of the inner gas volume and provides a safe electrical insulation for the central cathode, which divides the inner volume into two. A schematic drawing of the TPC concept is shown in Fig. 23.

Charged particles passing through the inner volume of the TPC ionize the gas molecules, and the liberated electrons drift away from the central cathode, towards the readout end plates. At the endplate, the electrons are amplified by gas electron multipliers, and signals are measured on pads roughly 8 mm square. The pattern of amplitudes and arrival times of the signals give precise information of the path of the charged particles, allowing for their momenta to be determined to better than about 10% for momenta below 1 GeV/c in the 0.2 T magnetic field provided by the UA1 magnet. The signal amplitudes themselves allow for good particle identification through dE/dx, giving good separation of electrons, protons, and muons/pions.

In order to verify that the T2K TPC concept will satisfy the performance requirements, a prototype

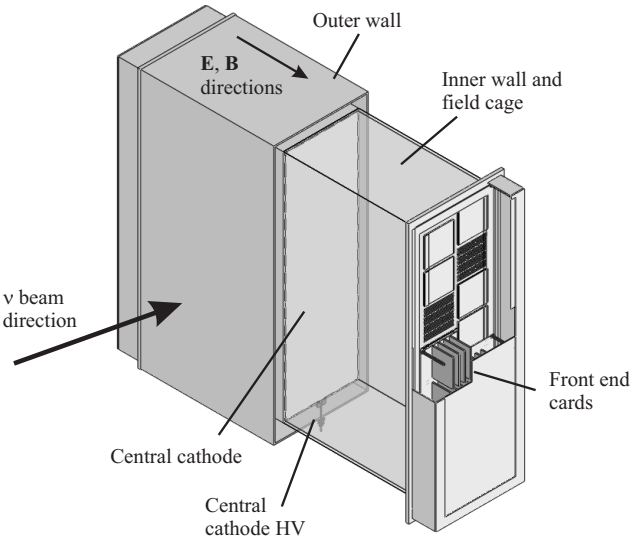

Fig. 23. Conceptual drawing of a TPC module is shown, with various pieces cut away to show the interior. Ionization electrons produced along the trajectory of charged particles in the inner volume drift towards the endplates and the amplified signals on pads are digitized by the front end electronics. The outer dimensions are approximately 2.5 m × 2.5 m × 1 m.

TPC module was designed and constructed in 2005 at TRIUMF, University of Victoria, and UBC. The prototype has two readout modules imaging a single gas volume with the full drift length of 1.25 m, as compared to the full size module that has 12 readout modules on each side of the central cathode. Large 30 cm × 30 cm GEM foils, produced at CERN, were used to build the two GEM readout modules, each consisting of 3 foils stretched onto frames to maintain a separation of 5 mm. Design drawings of the prototype are shown in Fig. 24.

The prototype includes aluminum strips on the central cathode, in order to test the use of a diffused UV laser to artificially generate tracks for calibration and distortion studies.

A flexible and safe high voltage distribution system was built for the prototype, allowing for monitoring of GEM currents. In order for the drift field to be as uniform as possible, the surface of the GEM that faces the drift volume is powered in common for both amplification modules on a single TPC endplate. This is also done for the other GEM layers. The potential across the GEMs is provided by individual isolated dc converters that use a low voltage input 0–12 V, and provide a proportional output voltage, 0–500 V. The voltage across the GEM and the current flowing through the GEM are monitored by isolated voltage and monitors. The failure of any supply will not cause the voltage across a GEM to exceed the safe operating range. Furthermore, the operating voltages and drift fields between GEMs can be adjusted, as needed.

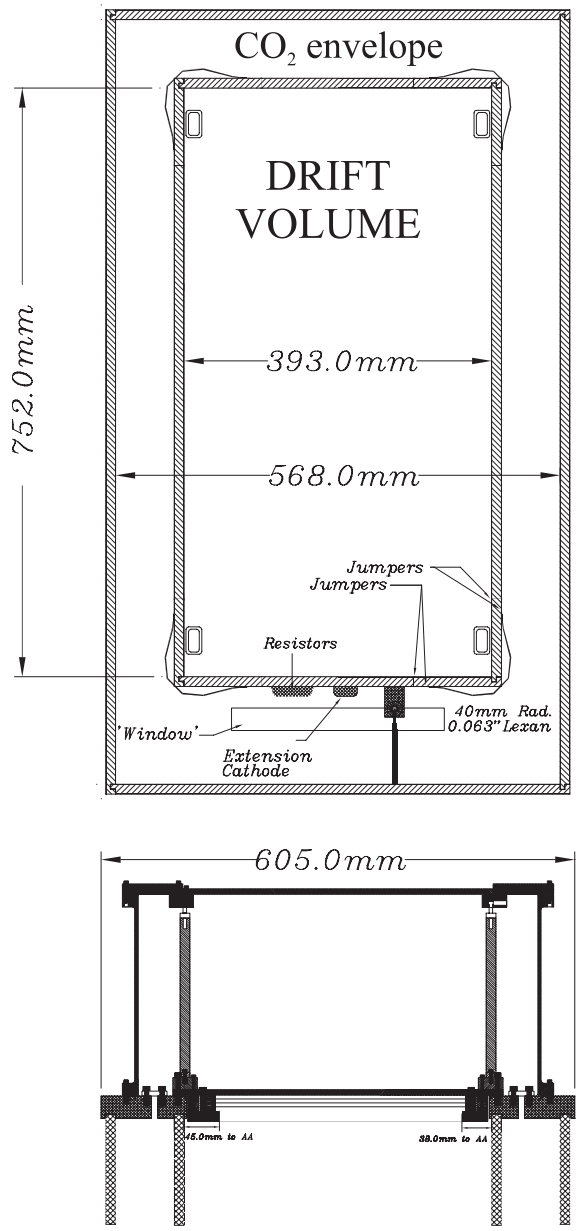

Fig. 24. End view design drawings of the prototype TPC. The figure shows the view inside the drift volume, showing the inner and outer walls. The inner box has rounded corners to prevent electrical breakdown. The lower drawing shows the detail of the triple GEM system.

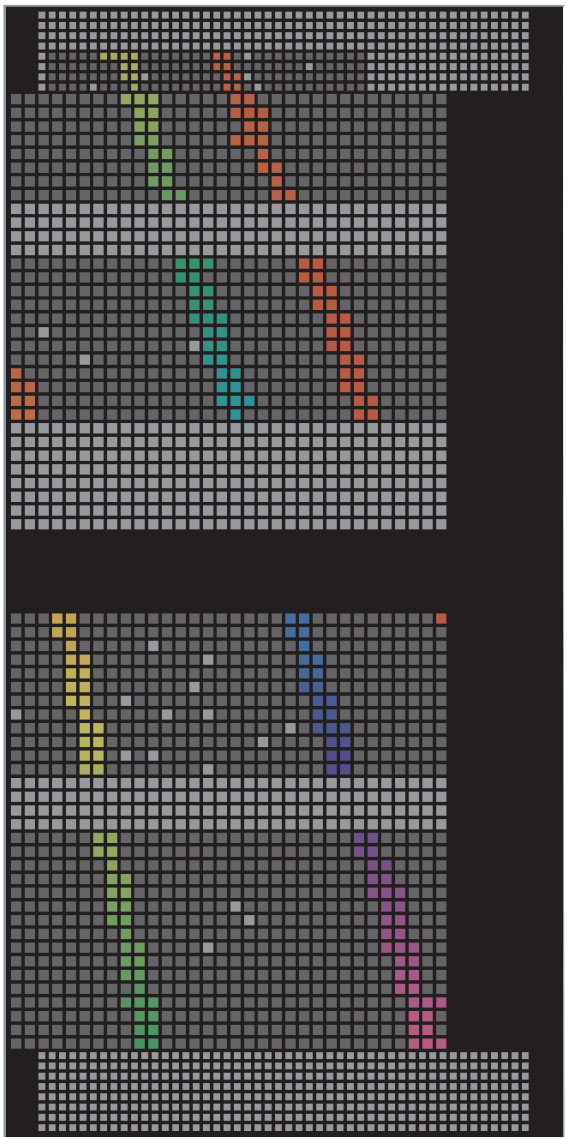

Fig. 25. An event recorded from the early tests of the TPC with 3 particles traversing the TPC. The coloured pads have signals above threshold, and the colour corresponds to the arrival time of the pulses. Light grey pads are not instrumented or not connected.

Readout electronics consisting of 2000 channels of 10 MHz/10 bit digitization were acquired from the ALICE TPC project at CERN for testing of the prototype.

The prototype TPC was brought into operation using Ar CO_2 (90:10) for the drift gas, and CO_2 for the gas envelope. The drift field was operated at 180 V/cm, and the GEMs were operated at a voltage of 340 V. A cosmic telescope was set up, allowing triggers from cosmic muons. Most events contain one muon crossing the TPC, however, some have several particles, such as the event shown in Fig. 25.

The preliminary analyses of many thousand cosmic ray events show that the principle design concepts of the TPC are sound, and that the spatial resolution goal for the device (roughly 0.7 mm per row of pads) is obtained.

In 2006, the Canadian T2K TPC groups will work to complete the design and construction of a full scale module, followed by the construction of the 3 production modules in the following two years, to be ready for their installation in Japan in early 2009.

K2K

Calibration source manipulator

(R. Helmer, TRIUMF)

To gain some experience with a running long baseline neutrino experiment and to test equipment and analysis techniques for T2K, a subgroup of the Canadian T2K collaboration joined the ongoing K2K experiment in 2003. The Canadian group was asked to participate in the optical calibration of the 1 kT near detector, with a view to investigating means of reducing some of the systematic errors in the prediction of the flux and spectrum at the far detector, Super-Kamiokande. The important optical parameters in the extrapolation include the absorption and attenuation lengths of the water, the photomultiplier tube (PMT) angular response, and the gains of the PMTs, all of which are used in Monte Carlo simulations to calibrate the energy scale and fiducial volume. These calibrations are even more important for ν_e appearance analyses in the two experiments. These analyses use the overall fit of the photon hit pattern to suppress π^0s misidentified as electrons. The main mechanism of misidentification is scattered light from the higher energy photon from the π^0 decay masking the Čerenkov ring from the lower energy photon. Thus, careful measurements of light scattering and attenuations are essential.

Three different systems have been used in the past for the optical calibration of the 1 kT detector. The first is a diffusing ball (the "laserball") which is pulsed with 384 nm wavelength light, giving a nanosecond burst of light and is used to measure PMT timing properties. The second is a scintillation ball excited by a xenon flasher giving a bright and isotropic light pulse, and is used to match the gains of PMTs. Third, a collimated laser beam is pulsed through the detector to provide a means of studying light scattering by looking at the PMTs perpendicular to the beam. Each system suffers from one or another defect. Because the light from the laserball is not emitted isotropically, it cannot be used to study the angular response of the PMTs. Light from the scintillating ball has a long pulse length so timing information cannot be used to separate photons that arrive at the PMTs without scattering from those that do. The direction of the collimated laser beam cannot be adjusted so that optical effects cannot be separated from possible anisotropies in the PMTs or detector. In addition, optical calibration source hardware could only be deployed on the central axis of the detector, and data were usually taken only at the detector centre.

In 2003, data taken by the Canadian group with the laserball at off-centre locations along the central axis showed significant reconstruction biases that were traced to flaws in the time vs. charge calibration. As a result of this work, a complete recalibration of the entire electronics chain was undertaken, significantly reducing these biases and hence estimation of the fiducial volume uncertainty. This work also raised the question of how the detector responded to other off-centre locations, and so the group undertook to build a manipulator system that would allow a much larger volume of the detector to be sampled. Data taken throughout the detector would also allow us to investigate the value of carrying out a SNO-style analysis, in which measurements taken at many locations and several wavelengths are used to unravel the optical response of the detector.

The manipulator consists of a 6 m long vertical column suspended in the detector from a platform mounted on the detector cover, with a three-jointed articulating arm mounted from the bottom of the column. Because of space limitations for insertion into the detector, the vertical section is made from three 2 m long segments. The articulating arm consists of two 2 m long inner segments and a shorter, 30 cm long, outer segment. The laserball is mounted at the outer end of this outermost segment. Four motors are used to rotate the column and drive the arm segments so as to position the ball in the desired location. The drive for each arm segment is transmitted from the mounting location at the top of the column via sprockets and drive chains. Figure 26 shows the motors and chain drives at

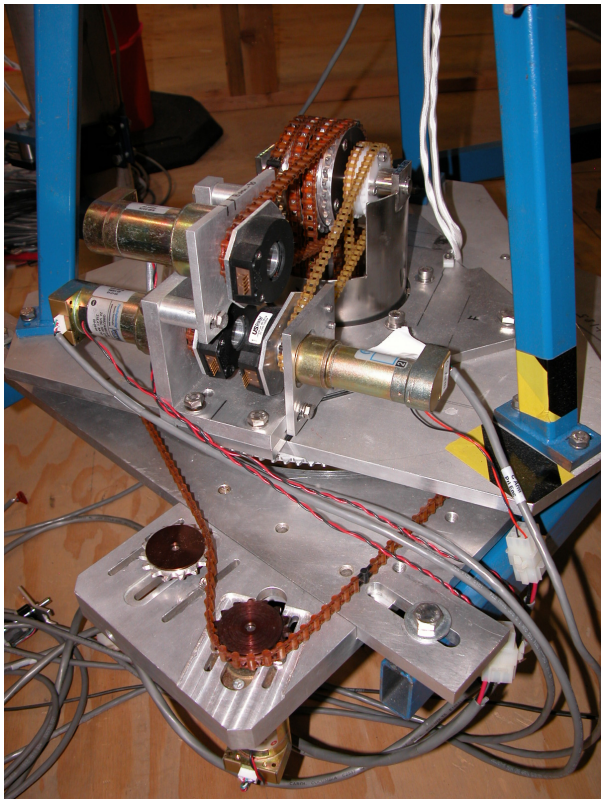

Fig. 26. The top end of the manipulator.

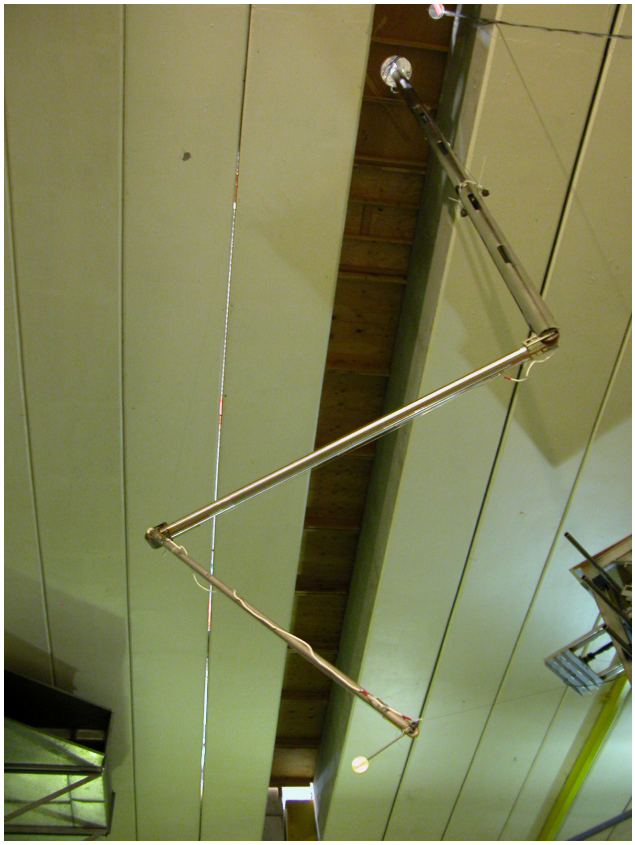

Fig. 27. The manipulator hanging in the proton hall.

the top of the manipulator. Each joint of the vertical section and arm conveys the drive to the next segment, until the arm segment being controlled is reached. To prevent contamination of the ultra-pure water in the detector, only stainless steel and some plastics were used in fabrication. To minimize the forces required to move the ball, the articulating arm segments are hollow and sealed at the ends so as to have neutral buoyancy. Figure 27 shows the column and movable arms while the manipulator was mounted in the proton hall for calibration.

It was of paramount importance to be able to position the source accurately and to prevent any impact between manipulator and detector components. A control system that incorporated innovative feedback of arm positions using submersible position sensors and redundancy in the feedback system was used to achieve these goals. The sensors used were solid state accelerometers based on MEMS technology. Their resolution permitted angles to be read to 0.1° accuracy. They were mounted in pairs on a small circuit board epoxied to each movable arm. Two pairs were also mounted on the vertical section to monitor deflection of the column in two planes.

Part of the redundancy of the readout system was accomplished by using one processor to read out one of the pairs of sensors on each arm, while a second processor read out the other sensor independently. In addition, all motors used to drive the arms have incremental optical encoders to provide position feedback and, as well, auxiliary encoders are mounted on each motor shaft. Thus there is four-fold redundancy in the position readback, and the safety system made use of this information to incorporate various measures to ensure the source was kept away from detector components.

Data from the arm motion sensors were read out using MIDAS and, in turn, three MIDAS front-end programs were used to control the arm motion. MatLab was used to build a graphical user interface for the system. The interface displayed views of the manipulator position that assisted the operator in visualizing arm movement and diagnosing any problems that were preventing arm movement.

Data were collected at more than 200 positions within the detector volume, and each position was sampled at low, medium, and high occupancy. Analysis of the data is under way.

Sudbury Neutrino Observatory
(R. Helmer, TRIUMF)

Production data-taking with the discrete ^{3}He counters in the detector started at the beginning of 2005. Analysis of this data is in progress. Although it is planned to continue taking data with these counters until the end of 2006, a preliminary result will be published based on data taken up to a cut-off date early in the year.

A paper in which the electron energy spectra, fluxes, and day-night asymmetries of ^{8}B solar neutrinos from the salt phase of SNO was published during the year. As noted in previous Annual Reports, the addition of 2 tonnes of salt to the heavy water enhanced the detection of neutral current (NC) interactions above that achieved with the heavy water alone. Most importantly, it allowed a statistical separation of charged-current (CC) events from other event types based on event isotropy criteria without any assumptions about the underlying neutrino energy spectrum. In addition, the neutron capture efficiency increased by nearly three-fold, allowing a precise measurement of the NC disintegration of deuterons by solar neutrinos. Finally, the observed energy spectrum of NC interactions is shifted upwards, thus providing better separation from low energy radioactive backgrounds.

The total flux of active-flavour neutrinos was found to be

$$\phi_{\rm NC} = 4.94 \pm 0.21({\rm stat})^{+0.38}_{-0.34}({\rm syst})$$

while the integral flux of electron neutrinos was

$$\phi_{\rm CC} = 1.68 \pm 0.06({\rm stat})^{+0.08}_{-0.09}({\rm syst}),$$

assuming an undistorted ^{8}B spectrum. The flux of neutrinos elastically scattered from electrons was found to be equivalent to an electron neutrino flux of

$$\phi_{\rm ES} = 2.35 \pm 0.22({\rm stat}) \pm 0.15({\rm syst}).$$

These results are consistent with those expected for neutrino oscillations with the large mixing angle parameters. A search for matter enhancement effects in the Earth through a possible day-night asymmetry in the CC integral rate was also carried out. No statistically significant asymmetry was observed.

A second publication was based on a search for periodicities in the ^{8}B solar neutrino flux. Periodic variations in the measured solar neutrino fluxes, putatively related to the solar rotational period, have been reported recently. SNO has unique capabilities to search for such periodicities based on its real-time detection, low backgrounds, and sensitivity to different neutrino flavours. In particular, it is possible to carry out an unbinned analysis in which the times of individual neutrino events are used as input, rather than the more usual analysis in which time bins of unequal size are used as inputs. The advantage of an unbinned analysis is that there is no possibility of periodicity-aliasing effects caused by the choice of bin size. Nevertheless, the more traditional Lomb-Scargle periodogram analysis with one day binning was also carried out for comparison with the other analyses. The analysis was based on data collected during the D_2O and salt phases of SNO.

The unbinned search was carried out at 3650 frequencies with periods ranging from 10 years down to 1 day. Comparison with 10,000 Monte Carlo sets generated with no periodicity showed there were no statistically significant periodicities in the SNO data set. Similarly, comparison of the Lomb-Scargle periodogram, generated at 7300 frequencies with periods ranging from 10 years to 2 days, with the Monte Carlo sets showed no evidence of time variability.

In addition to the above tests, searches for sinusoidal variations were carried out at two particular frequencies, one corresponding to a putative frequency of 9.43 yr^{-1} (and 7% amplitude) claimed for the Super-Kamiokande data (but not by the SK collaboration), and the other for the expected annual modulation of the neutrino flux by the Earth's orbital eccentricity. The amplitude for the former frequency was found to be $1.3 \pm 1.6\%$, and for the latter 0.0143 ± 0.0086, in good agreement with the expected value.

During the past year, TRIUMF's infrastructure support was limited to the lithium-8 source, for which TRIUMF has maintenance and operational responsibilities. The source was examined and cleaned. No refurbishment was necessary as it appeared to be in as good shape as it was the last time it was run (2002). It is planned to take data with the source early in 2006.

TJNAF Experiment 00-006
Measurement of the flavour singlet form factors of the proton ($G\emptyset$)
(W.T.H. van Oers, Manitoba)

The structure of the nucleon at low energies is not well understood in terms of the quark and gluon degrees of freedom. The $G\emptyset$ experiment will measure two proton ground state matrix elements which are sensitive to point-like strange quarks and hence to the quark-antiquark sea in the proton. The matrix elements of interest are the elastic scattering vector weak neutral current charge and magnetic form factors, G_E^Z and G_M^Z, respectively. These can be extracted from a set of parity-violating electron-proton scattering measurements. If one assumes a relationship between the proton and neutron structure, in that the proton and neutron differ only by the interchange of up and down quarks (i.e. charge symmetry), the strange quark (as well as the up and down quark) contribution to the charge and magnetic form factors of the nucleon can be determined. This results from taking appropriate linear combinations of the weak neutral form factors and their electromagnetic counterparts.

Determinations of both the charge and magnetic strange quark form factors are of fundamental interest, as these would constitute the first direct evidence of the quark sea in low energy observables. It is the objective of the $G\emptyset$ experiment to determine these contributions to the proton form factors at the few per cent level. Observations at high energy suggest that the strange quarks carry about half as much momentum as the up and down quarks in the sea. It is important to determine both the role of the quark sea and the relevance of strange quarks at low energy where there are voids in understanding the theory of the strong interaction (quantum chromo dynamics, QCD). The matrix elements, G_E^Z and G_M^Z, are also relevant to discussions of the Ellis-Jaffe sum rule and the pion-nucleon sigma term; there is uncertainty in both of these about the strange quark contributions. The $G\emptyset$ experiment will allow the determination of the strange contributions to the proton charge and magnetic form factors in a much more straightforward manner than is possible with regard to the corresponding observables in the above two deduced relations.

In the $G\emptyset$ experiment, which is being carried out in Hall C at the Thomas Jefferson National Accelerator Facility (TJNAF), parity-violating longitudinal analyzing powers will be measured in electron-proton scattering in the range $0.1 \leq {\rm Q}^2 \leq 1.0\ {\rm GeV}^2$ at both forward and backward angles. The longitudinal ana-

lyzing power is defined as

$$A_z = (1/P)\frac{[\sigma^+(\theta) - \sigma^-(\theta)]}{[\sigma^+(\theta) + \sigma^-(\theta)]}$$

where P is the polarization of the incident electron beam and the + and – signs indicate the helicity state. Making pairs of measurements at forward and backward angles will allow the separation of G_E^Z and G_M^Z. Predicted longitudinal analyzing powers range from about (–3 to –35) $\times$ 10^{-6}; the goal is to measure the longitudinal analyzing powers with statistical uncertainties of $\Delta A/A = 5\%$ and systematic uncertainties related to helicity correlated effects of $\Delta A/A \leq 2.5 \times 10^{-7}$.

The results of the $G\emptyset$ experiment running in the forward angle mode have been published in Physical Review Letters, August 26, 2005. It shows the first detailed picture of a mixture of G_E^s and G_M^s, which indicates that the strange quarks make a contribution to the proton's charge and magnetization distributions. About 5% of the proton's magnetic moment may come from strange quarks, although theoretical predictions give values ten times smaller. This discrepancy needs to be resolved by more extensive calculations.

The heart of the $G\emptyset$ detection system is a spectrometer which consists of an eight-sector toroidal magnet, with an array of scintillation detectors located at the focal surface of each octant and, for the backward angle mode, additional arrays of scintillation detectors and a Čerenkov detector located near the magnet cryostat-exit window of each octant. In the first phase of the experiment, longitudinal analyzing powers have been measured concurrently at several values of the momentum transfer in the range $0.1 \leq Q^2 \leq 1.0$ GeV^2. In the second phase of the experiment, each subsequent backward angle analyzing power measurement would require one month of continuous running time. The results of the SAMPLE experiment at the MIT-Bates laboratory have shown the importance of measuring the axial form factor corrections. Therefore, companion measurements of quasi-elastic scattering from deuterium will also be made at the backward angles. With these measurements, the effective axial current of the nucleon will also be determined. This current includes effects from the effective axial coupling of the photon to the nucleon or anapole moment, which are relevant also in other processes (e.g. atomic parity violation).

Considerable progress has been made in the design, prototyping, fabrication, testing, and installation of critical components for the second phase backward angle mode of the experiment. In particular, the cryostat exit detectors (CEDs), the aerogel Čerenkov detectors, and the mini-Ferris wheel support structure have been fabricated and installed onto the existing Ferris wheel detector support structure in Hall C. The Canadian contributions to these efforts have been significant. Below is an enumeration of the various Canadian contributions to the $G\emptyset$ experiment. The three components mentioned above as well as other aspects of the $G\emptyset$ experiment are described in some detail below.

Canadian contributions

The Canadian members of the $G\emptyset$ collaboration, based at the Universities of Manitoba, Northern British Columbia, TRIUMF, and the University of Winnipeg, have made the following contributions:

1. Develop and produce specialized photomultiplier tube bases for the focal plane detector arrays;
2. Design, build, and commission an automated magnetic field measuring (magnetic verification) apparatus complete with its own data acquisition system;
3. Prototype, fabricate and assemble the cryostat exit detector arrays for the backward angle measurements;
4. Prototype and fabricate (together with the Grenoble group) the aerogel Čerenkov arrays for background rejection in the backward angle measurements;
5. Design, fabricate, and assemble the support structure for the aerogel Čerenkov and cryostat exit detector arrays;
6. Provide additional electronics with the Čerenkov detectors to allow data-taking in multiple experiment mode;
7. Coordinate the implementation of TJNAF built beam monitors and control apparatus with TRIUMF built parity-type electronics; provide additional electronic modules for the backward angle measurements;
8. Provide support for the coordinating and scheduling of resources for $G\emptyset$ commissioning, engineering, and data-taking runs at TJNAF.

Photomultiplier tube bases and magnetic verification system The photomultiplier tube bases and magnetic verification system have been described in detail in past Annual Reports. Both of these construction projects have been successfully completed and the hardware was successfully operated during the $G\emptyset$ forward angle run.

The forward angle run

The $G\emptyset$ experiment ran in forward angle mode from December 1, 2003 to May 9, 2004. A good summary of the $G\emptyset$ forward angle run can be found in the last Manitoba Progress Report. At that time the analysis was still under way and only preliminary blinded data were available. Since then, the analysis has been

completed. The data were unblinded on April 15, 2005 at a $G\emptyset$ collaboration meeting at TJNAF, and the final results were officially released at a Jefferson Lab seminar on June 17, 2005. At the same time, the paper was submitted to Physical Review Letters and a preprint (nucl-ex/0506021) was posted to the Cornell arXiv server. In August, the article appeared in Physical Review Letters [Armstrong *et al.*, Phys. Rev. Lett. **95**, 092001 (2005)]. This paper was chosen to be featured in Physical Review Focus (focus.aps.org). The $G\emptyset$ experiment was also covered in the September 3–9, 2005 edition of The Economist [**376**, 72 (2005)].

The data on which the forward angle results are based were taken during 13 weeks of production running from February 9 to May 9, 2004. University of Manitoba personnel staffed a total of approximately 30 person-weeks of shifts. The experiment accumulated approximately 10 Tbytes of good production data corresponding to 701 hours of beam at 40 μA (101 Coulombs) on the liquid hydrogen target.

Principle of the experiment An overview of the $G\emptyset$ equipment is shown in Fig. 28. The 3 GeV electron beam enters from the lower right where it first encounters the $G\emptyset$ beam monitors. Continuing from right to left, one sees the liquid hydrogen target service module, the eight-sector superconducting magnet system (SMS), and the focal plane detectors mounted in the eight sector Ferris wheel structure between the SMS and the green wall. Longitudinally polarized electrons scatter from the liquid hydrogen target, and the spectrometer accepts recoil protons in the angular range 62° to 78° (corresponding to 15° to 5° electrons). The principle of the forward angle measurement is shown schematically in Fig. 29. The spectrometer magnet

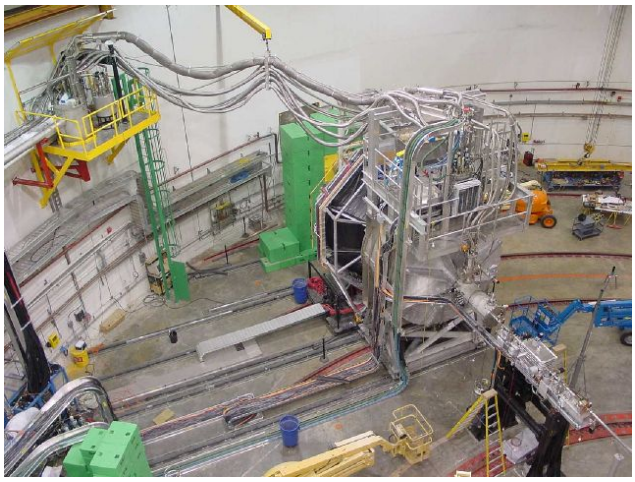

Fig. 28. The $G\emptyset$ apparatus installed in Hall C at TJNAF. The beam enters from the lower right. From right to left, we see the $G\emptyset$ beam monitoring girder, the LH_2 target service module, the 8-sector superconducting magnet, the detector Ferris wheel, and the green shielding wall.

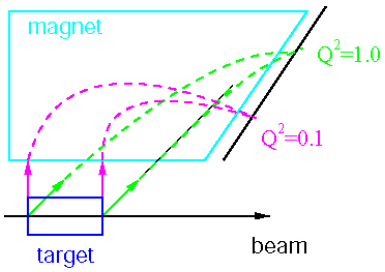

Fig. 29. Principle of the forward angle measurement. Recoil protons corresponding to a given momentum transfer are focused on a specific focal plane detector regardless of where in the target they originate.

is designed so that protons corresponding to a given momentum transfer (Q^2) are directed to a specific focal plane detector regardless of where in the target they originate. Q^2 from 0.16 to 1.0 $(\mathrm{GeV}/c)^2$ can be measured with one magnet setting. The experiment uses a beam time structure with beam bunches 32 ns apart. This is 16 times the usual TJNAF bunch spacing of 2 ns, and permits the protons from elastic scattering to be separated by time of flight from pions and inelastic protons.

Leakage beam measurement An unanticipated problem was the leakage of beam from the Hall A and B lasers. Hall A and B beams are 499 MHz, but the Hall C beam is 31 MHz. Unfortunately, the beam current monitors which are used to measure the charge asymmetry measure all the time and respond to the total A+B+C beam, whereas the $G\emptyset$ time-of-flight cut sees only the 31 MHz beam. This means that the correction for charge asymmetry was not right. We were able to measure the effect by looking in a forbidden region of the TOF spectrum where the signal could not come from the $G\emptyset$ beam bursts spaced at 32 ms (see Fig. 30). The leakage was typically 50 nA (c.f. 40 μA Hall C) with 340 ppm charge asymmetry. Corrections were made for the effects of beam leakage. The leakage correction is estimated to contribute $\sim$0.14 ppm systematic uncertainty.

Helicity correlated beam properties The helicity of the longitudinally polarized electron beam was selected every 1/30 second. The spins states were chosen in quartets, either $+--+$ or $-++-$, the first state of the quartet being chosen at random. Ideally, no other beam property would be affected, but in practice small changes in beam properties other than helicity occur. Thanks to good design practices such as cylindrical symmetry, the sensitivity of the experiment to helicity correlated beam properties was very small. Nevertheless, it was necessary to constantly monitor helicity correlated beam properties and to correct for the resultant false asymmetry. Table II shows the helicity correlated beam parameters for the forward

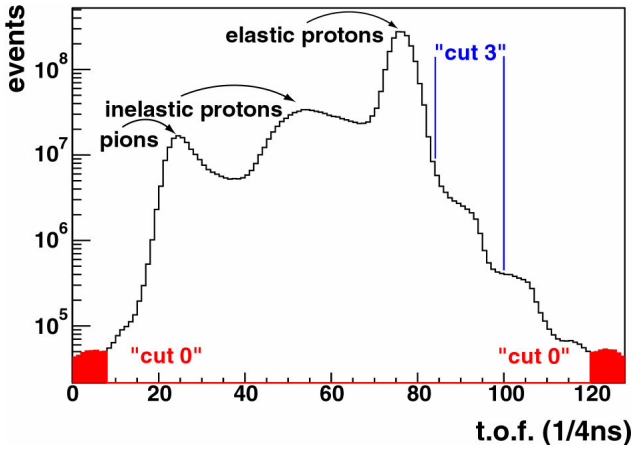

Fig. 30. Measurement of leakage beam. Some electron beam released by Hall A and B lasers at ion source was found to be leaking into Hall C. Leakage beam was small, about 50 nA compared to the $G\emptyset$ 40 μA main beam, and had the 499 MHz time structure of Halls A and B rather than the 31 MHz Hall C beam. We measured the leakage yield in the cut0 region where no true $G\emptyset$ beam exits.

Table II. Helicity correlated beam properties for forward angle production run compared to $G\emptyset$ specifications. These must be multiplied by sensitivity to these quantities to give the false signal. Numbers are slightly better than reported last year and reflect results of final analysis.

Beam parameter	Achieved	Specification
Charge asymmetry	-0.14 ± 0.32 ppm	1 ppm
x position difference	3 ± 4 nm	20 nm
y position difference	4 ± 4 nm	20 nm
x angle difference	1 ± 1 nrad	2 nrad
y angle difference	1.5 ± 1 nrad	2 nrad
Energy difference	29 ± 4 eV	75 eV

angle data. Charge and position feedback were used. The helicity correlated beam properties are all very small and, taken together, only produced a false asymmetry of $\sim$0.02 ppm.

Statistical properties of the data Figure 31 shows an asymmetry distribution for the forward angle data. The distribution is very clean over 5 decades.

Correction for background The measured asymmetry is a weighted sum of the true elastic asymmetry and the asymmetry of the background:

$$A_{\rm meas} = f_{\rm el} A_{\rm el} + f_{\rm back} A_{\rm back} \, .$$

To correct for the background, we must know both the background fraction, $f_{\rm back}$, and the asymmetry, $A_{\rm back}$, under the elastic peak. Figure 32 illustrates how these numbers were determined. We first fit the yield spectrum with a Gaussian peak plus a fourth order polynomial background and extracted the background fraction. We then fit the asymmetry spectrum with a second order polynomial and extracted the asymmetry of the background under the elastic peak. We tried several

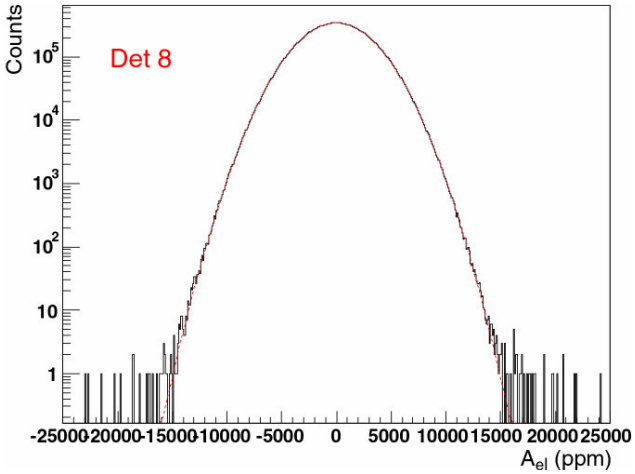

Fig. 31. High quality of the forward angle data. The asymmetry distributions were very clean over 5 decades.

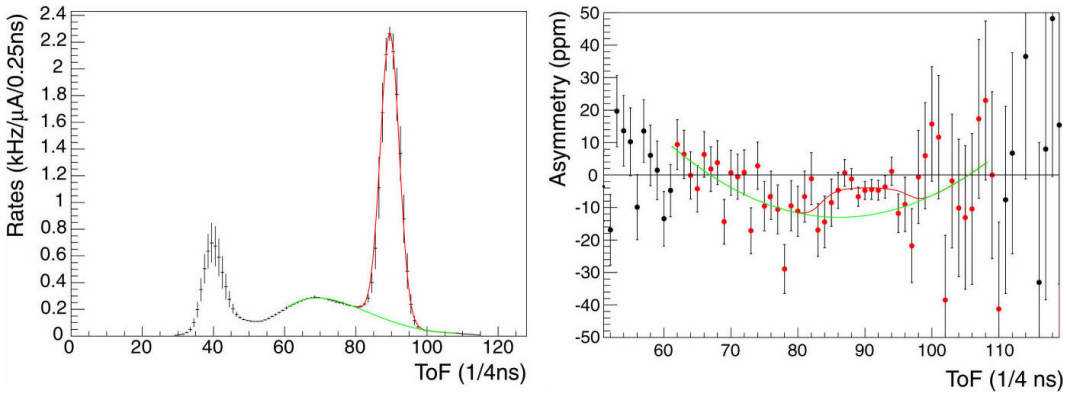

Fig. 32. Fitting of the yield and the asymmetry. In left panel the background under the elastic peak is shown fitted with with a fourth order polynomial and the peak itself with a Gaussian. The background asymmetry (right panel) is fitted with a second order polynomial.

Table III. Sources of systematic error. The table shows the source of the error, the correction made for the error, and the uncertainty introduced by making the correction.

Source	Correction	Uncertainty
Deadtime	0.05 ppm	0.05 ppm
Helicity-correlated beam properties	0.02 ppm	0.01 ppm
Leakage beam	0.71 ppm	0.14 ppm
Beam polarization	73.7%	1%
Background	–1 to +42 ppm	0.2 to 9 ppm

different, but reasonable, fitting methods and used the variation in results to assign a systematic uncertainty to the background correction, which was the dominant source of systematic error. This and the other sources of systematic error are summarized in Table III.

Final results The final analyzing powers obtained by the $G\emptyset$ forward angle run after all corrections are plotted as a function of Q^2 in Fig. 33. The inner error bars are statistical only, whereas the outer error bars are statistical plus systematic errors that affect only that point. Global systematic errors that would affect more than one point in a correlated way are shown by the grey band. The solid curve is the asymmetry expected for "no vector strange". It is calculated using the parameterization of Kelly [Phys. Rev. **C70**, 068202 (2004)] for G_E and G_M and assuming that G_E^s and G_M^s are zero. Since the data shown on Fig. 33 are taken at forward angles only, they determine a linear combination of G_E^s and G_M^s. Figure 34 shows the combination $G_E^s + \eta G_M^s$. (η is approximately 0.9 Q^2 here.) Shown are the $G\emptyset$ data and two points from the Hall A parity experiment, HAPPEX. One sees that the agreement

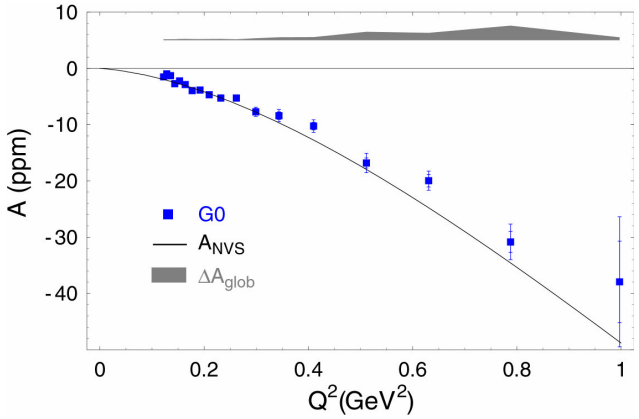

Fig. 33. Experimental analyzing powers measured by $G\emptyset$. The inside error bars are statistical and the outside error bars include point-to-point systematic errors. The grey band shows global systematic errors that affect more than one point. The solid line is the no vector strange curve calculated using Kelly's values for G_E and G_M and assuming that G_E^s and G_M^s are zero.

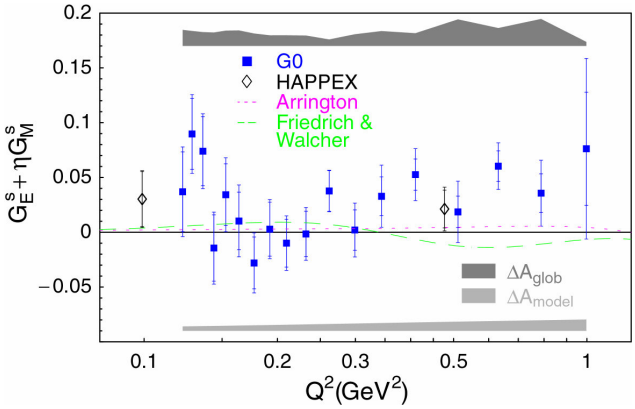

Fig. 34. Strange quark contribution to the charge and magnetization of the proton. Experiments at one scattering angle measure a linear combination of G_E^s and G_M^s. The hypothesis that strange quarks make no contribution is disfavoured at 89% confidence. See the text for an explanation of the dotted and dashed curves.

with the HAPPEX data is good and that the points do not appear to be consistent with no strange quark contribution. Because of the correlated uncertainties, a simple χ^2 test will not work here. To get around this, the data analysis team generated multiple copies of the data drawing the point-to-point and correlated errors from appropriate distributions. They found that in only 11% of the cases was the departure from no vector strange worse than the real data. We conclude that the no vector strange hypothesis is excluded with 89% confidence.

The departure of the data from the no-vector-strange case depends somewhat on the values used for the electromagnetic form factors G_E and G_M. The plotted points are calculated using Kelly's parameterization [Kelly, *op. cit.*]. The Arrington [Phys. Rev. **C69**, 022201(R) (2004)] (dotted red) and Friedrich and Walcher [Eur. Phys. J. **A17**, 79 (2004)] (dashed green) curves show how much the points would move if these other parameterizations were used. The new value of $G_E^s + \eta G_M^s$ for a given point is the distance from that point to the curve in question.

Combining $G\emptyset$ with other experiments By combining experiments at the same Q^2 but different scattering angle it is possible to separate the contributions of G_E^s and G_M^s. Figure 35 shows the world data at $Q^2 = 0.1$ $(GeV/c)^2$ assuming the Kelly form factors. The $G\emptyset$ data have been extrapolated to 0.1 $(GeV/c)^2$ using our first three data points. One sees that the favoured values of G_E^s and G_M^s are non-zero. The contours outline regions of 68% and 95% confidence.

Progress for the backward angle run

Cryostat exit detectors For the backward angle second phase of the $G\emptyset$ experiment, the addition of a second array of scintillation detectors, located near the

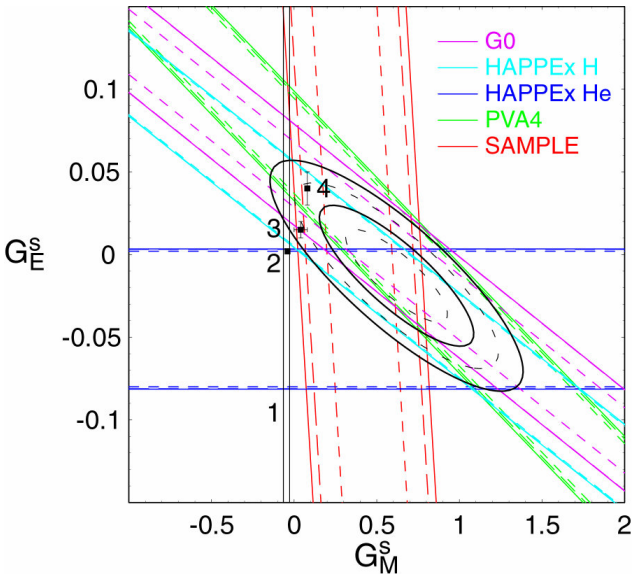

Fig. 35. World data at 0.1 $(\mathrm{GeV}/c)^2$. Different experiments constrain different linear combinations of G_E^s and G_M^s. Ellipses show the 68% and 95% confidence contours.

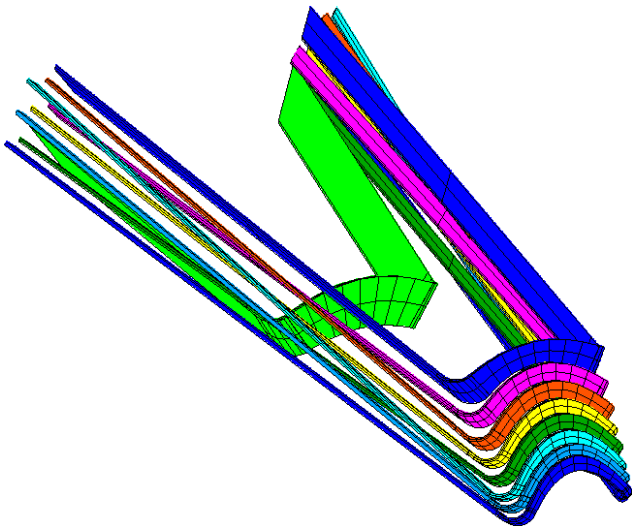

Fig. 36. Layout of a cryostat exit detector (CED) array for a single octant.

spectrometer-cryostat exit windows, is required in order to separate the elastic and inelastically scattered electrons. The geometry of these cryostat exit detector (CED) arrays (see Fig. 36) was studied in detail and a reference design was produced by the $G\emptyset$ simulation group. With the resident expertise at TRIUMF in producing high quality scintillation detectors and lightguides, the Canadian subgroup was asked to play the lead role in the prototyping and production of the CEDs. A set of prototype CEDs was built at TRIUMF and delivered to the $G\emptyset$ collaboration for studies with cosmic rays. Results from these studies showed that the reference design and the prototype detectors met the specification requirements for these arrays and construction of the production CED arrays began at TRIUMF. Fabrication of the CED scintillators for all 8 octants was completed and delivery was made to TJNAF, and fabrication of the special helical-bend lightguides began in 2002. In order to achieve the unique helical bend required in the $G\emptyset$ backangle geometry, customized bending jigs were designed and constructed at TRIUMF and tested on a first set of prototype CED lightguides. Production of a full set of lightguides for the first CED octant was completed with delivery to TJNAF in 2003, where they underwent further tests. Production of the lightguides for all 8 octants was completed with delivery to TJNAF in early 2004. The CEDs also make use of the same types of photomultiplier tubes and specialized TRIUMF/$G\emptyset$ bases as the focal plane detectors.

Aerogel Čerenkov detectors Monte Carlo simulation results showed that backgrounds from negative pions will be problematic for the backward angle measurements involving the deuterium target. The $G\emptyset$ Simulation subgroup focused on characterizing this π^- background and provided options for the design of an additional set of pion-rejection detectors. The $G\emptyset$ Canadian and French (Grenoble) subgroups were asked to jointly undertake the prototyping and construction of this crucial set of detectors, which will be made up of an array of aerogel Čerenkov counters.

A first set of prototype detectors, using borrowed aerogel samples, was constructed in 2001 and tested in the TRIUMF pion beam (M11) in late 2001 and 2002. In 2003, the sample aerogel in the prototype detector was replaced by a first batch of production aerogel, and the photon yield (and detector efficiencies) immediately improved. Average yields of approximately 12, 8, and 6 photoelectrons were observed for measurements made at the near, centre, and far ends of the Čerenkov diffusion box (positions were defined relative to the Čerenkov PMT positions).

Based on the results with the first prototype detector, a second iteration prototype (see Fig. 37) was designed and became the production version of the Čerenkov detector. Construction of four Canadian Čerenkov detectors (there are also four French Čerenkov detectors) was completed by the fall of 2004 and three of the detectors were delivered to TJNAF. The fourth detector remained at TRIUMF for further in-beam tests, carried out in 2004 and early 2005, using the M11 muon/pion beam line. Figures 38 and 39 show the electron efficiencies and the pion-rejection factors for the production detectors, respectively. The fourth Canadian Čerenkov detector was delivered to TJNAF in the summer of 2005.

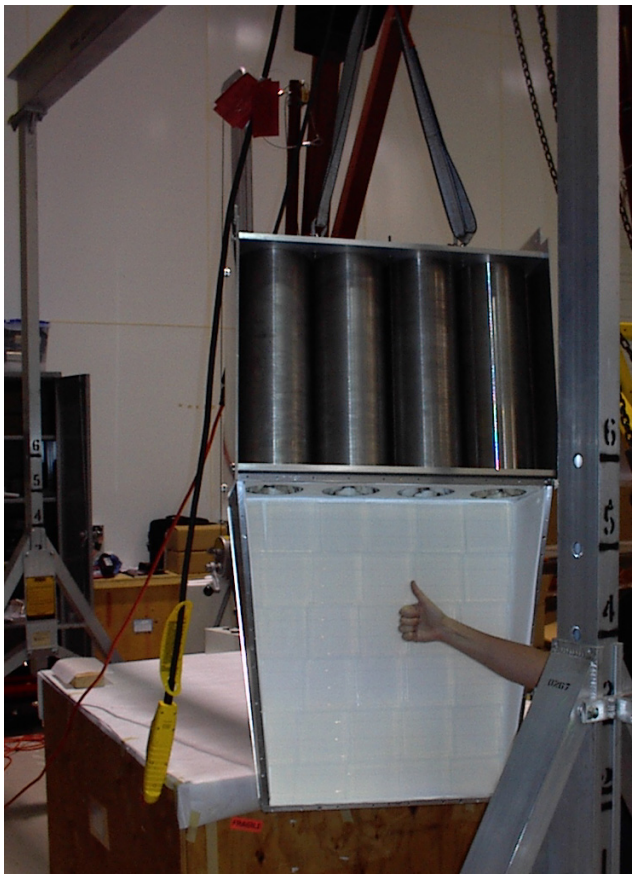

Fig. 37. The production version of the aerogel Čerenkov detector after arrival at TJNAF. The box is filled with aerogel tiles and the tile-retainer system has been installed.

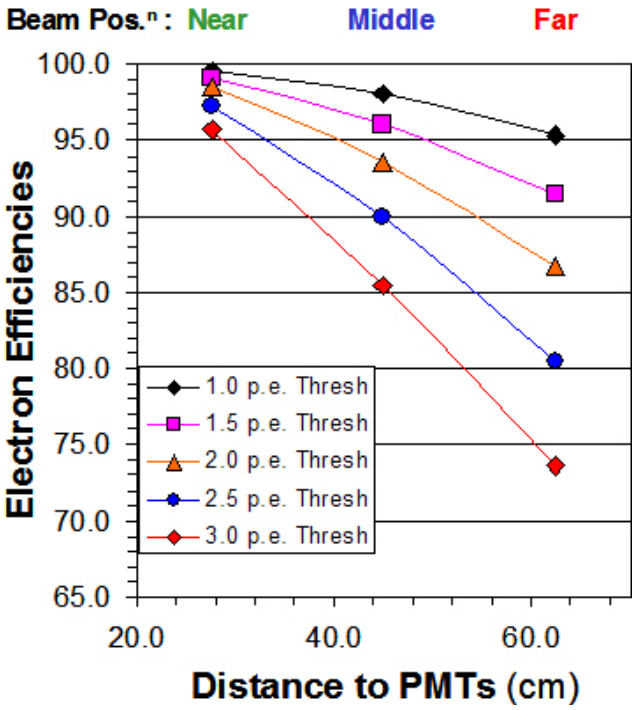

Fig. 38. The position-dependent efficiencies of the aerogel Čerenkov detector for various threshold settings.

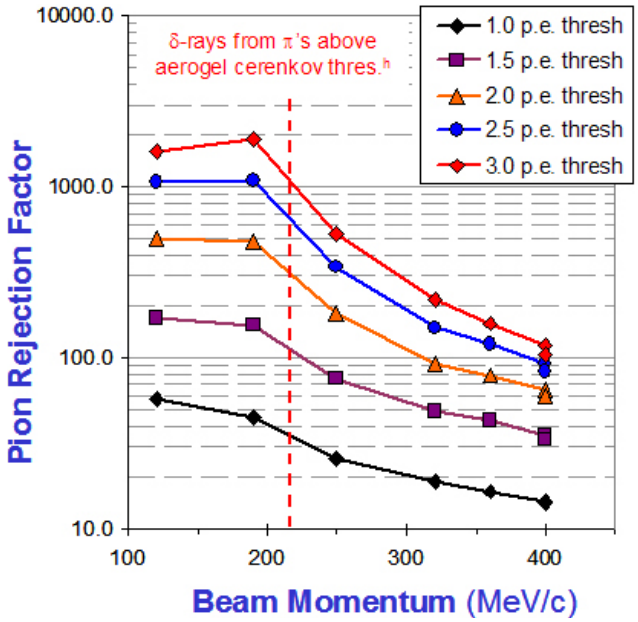

Fig. 39. The Čerenkov detector pion-rejection factors as a function of beam energy, for various threshold settings.

Electronics for backward angle mode of the $G\emptyset$ experiment Lessons learned from the completed forward-angle run of the $G\emptyset$ experiment led to a significant redesign of the electronics for the backward-angle run. In the forward-angle run, time of flight was used to distinguish elastically scattered protons from pions and inelastically scattered protons. The start for the time-of-flight measurement was a signal delivered by the arrival of beam at an rf cavity close to the target. This necessitated the use of an electron beam pulsed at 31 MHz. The usual Jefferson Lab beam structure is 499 MHz (continuous beam), so only one in sixteen rf buckets was filled in order to achieve 31 MHz. However, a small amount of beam always occupies every available bucket. This beam arises from simultaneously running continuous beams for the two other experimental halls. This resulted in false asymmetries from so-called leakage beam. Fortunately, normally unpopulated sections of the time-of-flight spectrum could be used to correct for the effects of the leakage beam.

Originally, the backward-angle experiments would also have used 31 MHz beam, in order to reuse electronics from the forward-angle experiment. However, owing to the leakage beam asymmetries encountered in the forward-angle experiment, continuous beam will be used for the backward-angle run. The backward-angle experiments do not use the time-of-flight technique for particle identification purposes, instead relying on the Čerenkov counters. The use of continuous beam is therefore feasible and necessary, due to the lack of ability to use the forward-angle correction scheme. The result of this change is that the experiment must

provide its own trigger signals, and additional electronics are required.

New front-end electronics were required to make use of the Canadian Čerenkov counters in a way consistent with the new trigger scheme for the experiment. The electronics in question are crucial for trigger generation, for on-line calibration of the Canadian Čerenkov counters, and for pion contamination studies. The electronics are also necessary to give sufficient flexibility to have the Čerenkov signals arrive in time with signals from the other detectors used in the experiment (scintillation counters with faster time-response).

The final electronics design studies were concluded in spring, 2005. The new electronics purchased over summer 2005 were two VME leading-edge discriminators, and four VME analogue sum/splitter modules.

Backangle support structure Considerable effort has gone into the engineering design of a support structure for the $G\emptyset$ Čerenkov and CED arrays. Although the Canadian subgroup was initially responsible only for the design of the Čerenkov support structure, it was soon realized that the CED support structure would be closely coupled to the former due to the physical proximity of the two detector subsystems. As such, it was later decided than an integrated design for the two detector subsystems should be pursued. The support structure centres around the use of prefabricated aluminum extrusions from Bosch because of their strength, versatility, and relatively low costs. A series of detailed finite-element analysis studies was carried out at TRIUMF, using the program ANSYS, to identify potential problems and to optimize the strength and cost of the support structure. The design consists of a second Ferris wheel type support structure (the mini-Ferris wheel), which couples to the existing detector support structure (also a Ferris wheel type design) and to the linear rails on the existing $G\emptyset$ detector platform. A conceptual illustration of the $G\emptyset$ backward angle configuration is shown in Fig. 40, with the superconducting magnet, the 3 detector arrays (FPD, CED, Čerenkov) in each of the 8 sectors, and their respective support structures.

Over spring, 2003, the parts for a single octant of the support frame were procured and successfully assembled at TJNAF (see Fig. 41). As various components of the backward angle detectors arrived at TJNAF over the summer of 2003, work began on a test assembly of one octant of the backward angle system to validate the overall design and assembly procedure. In particular, the scintillators themselves could only be directly supported by a low-density material. Furthermore, the CED scintillators had to be glued, *in-situ*, to their respective lightguides and any potential interferences between adjacent detectors would have to

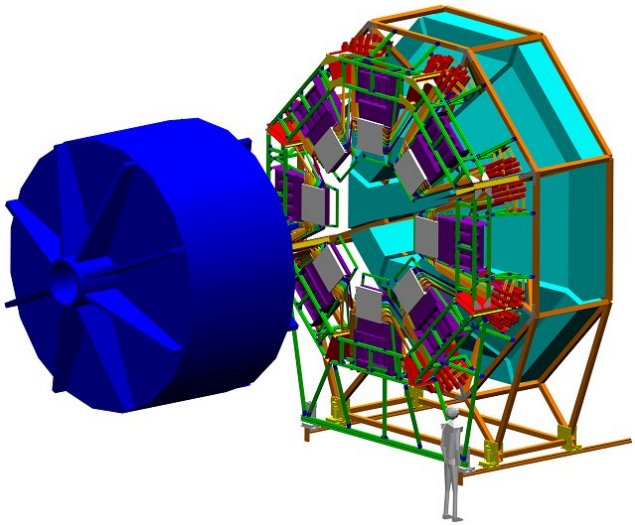

Fig. 40. Conceptual layout of the $G\emptyset$ backward angle configuration.

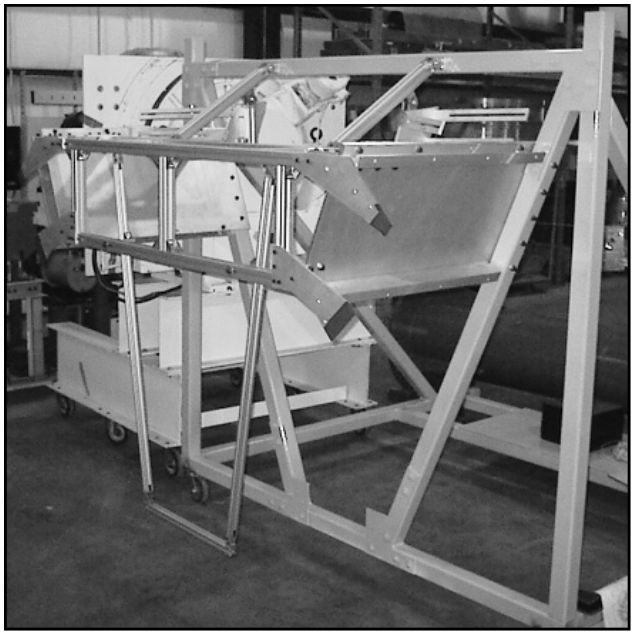

Fig. 41. A single octant of the backangle detector support frame.

be identified and reconciled. An assembly to locate and hold the CED scintillators was designed and built. This assembly was constructed from a structural foam material, Rohacell-71, which is light-weight ($\approx$71 g/cm^3) and easily machinable. In late 2003, the test assembly was completed and the overall support frame design was validated. Assembly of all eight backangle detector support octants was completed in late fall 2004 at TJNAF.

Installation of backward angle detector system and cosmic ray tests Concurrent with the assembly of the backangle support octants, *in-situ* assembly

(mounting, glueing, and light-sealing) of the cryostat-exit detectors, on the backangle support octants, began in 2004. In April, 2005, assembly of all eight octants of the CEDs was completed. Upon completion of each CED octant, cosmic ray tests were carried out to help characterize these detectors and to identify problematic detectors and/or glue joints. These tests focused on establishing the light yield as a function of hit location along the length of each detector, and were carried out by measuring the number of photoelectrons for each event in the left and right PMTs of each CED. As well, timing measurements in both left and right CED PMTs were carried out, relative to a set of reference trigger detectors. As a result of these tests, a number of problematic detectors were identified and replaced or reglued. Presently, all of the CEDs have a light yield that is reasonably high and uniform over the length of the detector.

In April, 2005, mounting tests using a first set of Canadian and French Čerenkov detectors were carried out. Mounting of all eight octants of Čerenkov detectors was completed in July. During this period, an octant lifting and rotation jig, designed at TJNAF for lifting, rotating, and positioning each backangle octant onto the main $G\emptyset$ detector Ferris wheel, was assembled in the EEL cleanroom and prepared for an initial set of rotation tests. These rotation tests were carried out in July, and a 360° rotation was successfully completed for one backangle octant. As part of the rotation test procedure, the octant was held upside down over night for the purpose of a prolonged stress test (see Fig. 42).

A first set of integrated CED-Čerenkov detector tests was carried out in August. In these tests, left-right time differences from the CED TDCs were used to define localized regions of the Čerenkov detectors. Figure 43 shows the TDC difference between Čerenkov PMT-1 and the right PMT on CED-8. The mean time difference recorded in the DAQ is about −88 ns (−365 ch). As there was a 100 ns delay built into the data-acquisition system, the time difference at the PMT outputs is about 12 ns. These initial timing tests were carried out without the postamp stages attached to the Čerenkov PMT outputs.

In early November, the 8 fully-assembled detector octants were moved from the EEL cleanroom at TJNAF into Hall C. They were then installed, one octant at a time, onto the existing detector support structure, to form the front-end mini-Ferris wheel subsystem (see Fig. 44). Presently, all of the detectors installed in the double Ferris wheel system are undergoing yield and timing tests making use of cosmic rays.

Future In March, 2006, the $G\emptyset$ backangle commissioning run will begin, followed by the first backangle production run in April, 2006. It is expected that a

Fig. 42. A single backangle octant, complete with CEDs and Čerenkov detector installed, rotated by 180° into the octant-5 orientation.

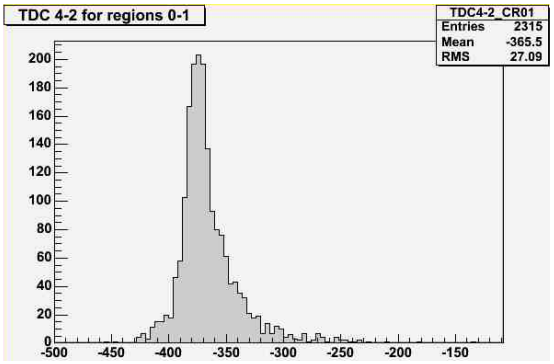

Fig. 43. A TDC spectra showing the relative timing between Čerenkov PMT-1 and the right PMT on CED-8.

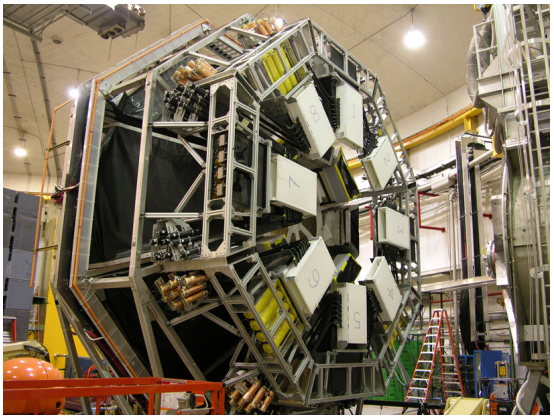

Fig. 44. The fully-assembled mini-Ferris wheel structure supporting the front-end detectors is shown mounted onto the existing Ferris wheel detector support structure.

second production run will take place in late summer, 2006, followed by further production runs in late 2006 and early 2007.

Canadian subgroup of the $G\emptyset$ collaboration: J. Birchall, M. Choi, W.R. Falk, C. Enderud, M. Gericke, L. Lee, S.A. Page, W.D. Ramsay, G. Rutledge, W.T.H. van Oers (Manitoba); E. Korkmaz, T. Porcelli (UNBC); J.W. Martin (Winnipeg); C.A. Davis (TRIUMF).

TJNAF Experiment 02-020

The Q_{weak} experiment: a search for physics at the TeV scale via a measurement of the proton's weak charge

(S.A. Page, Manitoba)

At forward angles and low momentum transfer, the parity violating longitudinal analyzing power in $\vec{e}p$ elastic scattering is given by $A_z = \frac{G_F}{4\pi\alpha\sqrt{2}}(Q_w^p Q^2 + BQ^4)$, where Q_w^p is the weak charge of the proton and Q is the momentum transfer. The first term in the expression for A_z is for a pointlike proton. The second term contains corrections for the hadronic form factors. At low Q^2, the first term dominates and A_z is a measure of the weak charge of the proton. The Q_{weak} experiment will run at $Q^2 = 0.03$ $(\mathrm{GeV}/c)^2$ and make small corrections for the hadronic form factors based on the results of the HAPPEX, , PVA4, and SAMPLE experiments. Q_{weak} plans to measure the predicted A_z of –0.3 ppm with a combined statistical and systematic uncertainty of 2.2%, corresponding to a total uncertainty of 4% in Q_w^p. At tree level in the standard model, $Q_w^p = 1 - 4\sin^2\theta_w$, where θ_w is the weak mixing angle. Since $\sin^2\theta_w$ is so close to 1/4, a 4% measure of Q_w^p determines $\sin^2\theta_w$ to 0.3%.

Figure 45 shows how $\sin^2\theta_w$ is predicted to vary with the momentum transfer at which it is measured – referred to as the "running" of $\sin^2\theta_w$. Note that smaller $\sin^2\theta_w$ corresponds to larger weak coupling, and that momentum transfer Q corresponds to a distance scale 1/Q. The rise in $\sin^2\theta_w$ below the Z-pole is due to virtual fermion pairs screening the weak charge, causing it to appear smaller at larger distances. Above the mass of the W, boson pairs introduce anti-screening and the observed weak charge falls at shorter distances. The electroweak radiative corrections which give rise to these changes depend not only on known particles, but also on particles which have not yet been discovered. A discrepancy between the measured value and the calculated value may signal new physics. Our proposed measurement of Q_w^p to 4% will be sensitive to new physics at the few TeV scale. Also shown on Fig. 45 are the results of other measurements, including that of the SLAC E158 Möller scattering experiment, released in 2005.

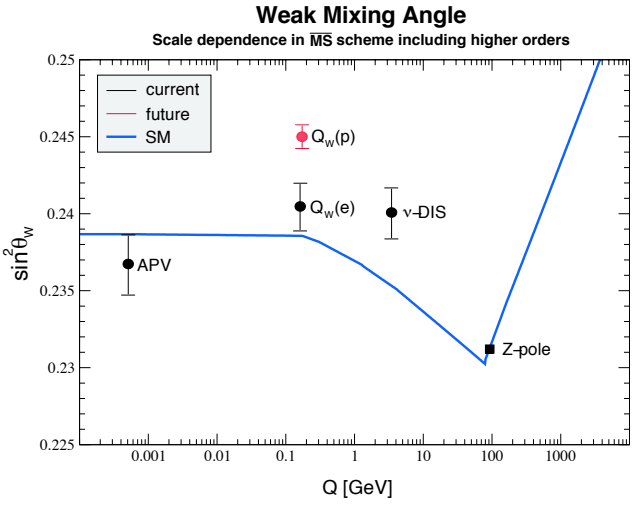

Fig. 45. Calculated running of the weak mixing angle in the standard model. The data points shown are those from the atomic parity violation experiment on Cs (APV), the SLAC E158 experiment ($Q_w(e)$), the Fermilab NuTeV experiment (ν-DIS), and from several leptonic and semi-leptonic experiments at the Z^0 pole. Also shown is the anticipated error bar of the Q_{weak} experiment at Jefferson Lab.

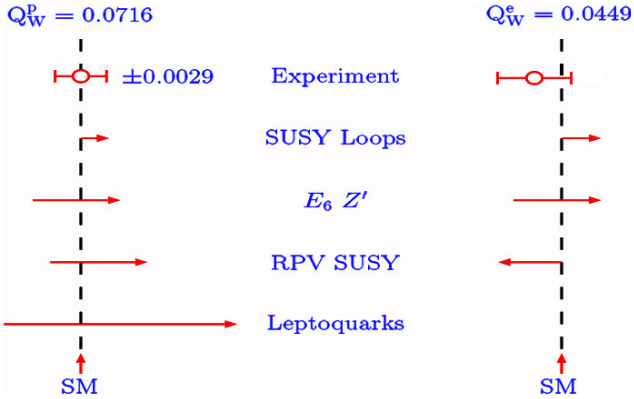

Fig. 46. A comparison of the anticipated error for the Q_{weak} (Q_W^p) experiment and the result of the SLAC E158 (Q_W^e) experiment published in 2005. The dotted lines are the standard model values and the arrows show the effects of various new physics additions to the standard model that are allowed by fits to existing data at a 95% confidence level. SUSY loops and a 1 TeV Z' would have effects in the same direction for both measurements and could result in evidence for new physics. RPV SUSY has effects in opposite directions. Only Q_W^p is sensitive to leptoquarks.

The SLAC E158 electron result is particularly interesting because its sensitivity to new physics is complimentary to that of our proton experiment. Figure 46 illustrates how different extensions to the standard model would affect the two measurements in different ways. For example, only Q_w^p is sensitive to leptoquarks.

Experiment overview

Table IV outlines the basic parameters of the Q_{weak}^p experiment. The experiment will measure the parity violating asymmetry in polarized electron-proton

Table IV. Basic parameters of the Q^p_{weak} experiment. Averages are cross section and acceptance weighted.

Parameter	Value
Incident beam energy	1.165 GeV
Beam polarization	85%
Beam current	180 μA
Target thickness	35 cm ($0.04X_0$)
Running time	2200 hours
Nominal scattering angle	8.4°
Scattering angle acceptance	$\pm 3°$
ϕ acceptance	53 % of 2π
Solid angle	$\Delta\Omega = 45.7$ msr
Averaged Q^2	0.03 (GeV/c)^2
Averaged physics asymmetry	–0.288 ppm
Averaged experimental asymmetry	0.24 ppm
Integrated cross section	3.9 μb
Integrated rate (all sectors)	6.4 GHz
Statistical error on the asymmetry	1.8%
Statistical error on Q^p_W	2.9%

scattering at very low momentum transfer (Q^2 = 0.03 (GeV/c)^2) and an energy of 1.12 GeV. These experimental conditions will suppress the hadronic form factor contributions to the measured asymmetry. A toroidal magnetic field from an eight-sector spectrometer magnet will focus elastically scattered electrons onto a set of eight, rectangular synthetic quartz Čerenkov detectors coupled to photomultiplier tubes, which will be read out in current mode to achieve the high statistical precision required for the measurements. A 2200 hour measurement using 180 μA of 80% polarized beam on a 0.35 m liquid hydrogen target will determine the proton's weak charge with a 4% combined statistical and systematic error.

The Manitoba/TRIUMF/UNBC/Winnipeg group is leading the magnetic spectrometer construction project and is designing, developing, and fabricating the electronics for the main detector system. Further responsibilities of the group are in systematic error evaluations, in beam line monitoring and control apparatus, and in the detection system for the Compton polarimeter.

The Q_{weak} magnetic spectrometer QTOR

The resistive toroidal magnet with eightfold symmetry has been defined by the magnet working group in various meetings held at TRIUMF, Jefferson Lab, and Louisiana Tech in which physicists and engineers from Jefferson Lab, Louisiana Tech, Manitoba, MIT-Bates, and TRIUMF participated. The magnet, the coil holders, and the support structure have been designed at MIT-Bates. Figure 47 shows the magnet coils mounted on their support structure.

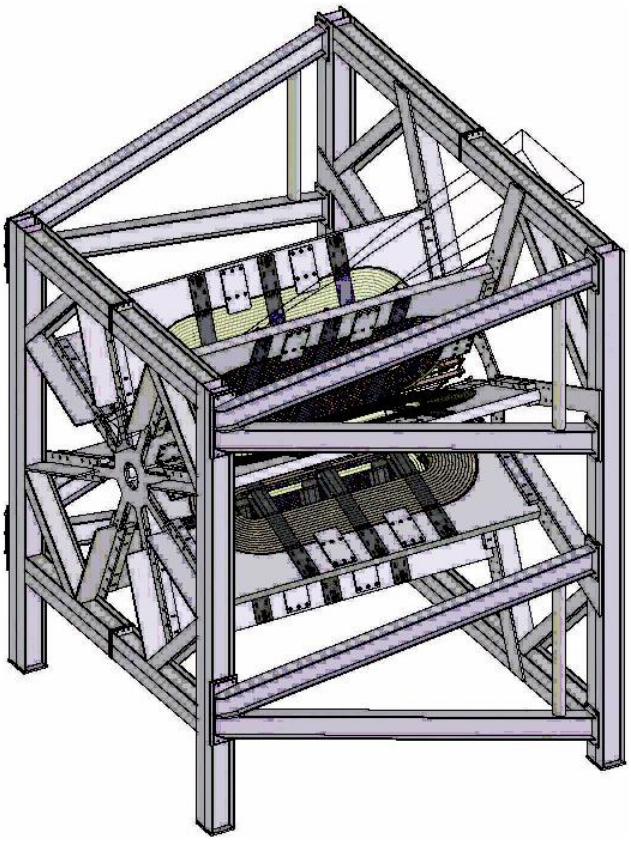

Fig. 47. Three-dimensional view of the Q_{weak} resistive toroidal magnet with its support structure. Fabrication of the coils and coil holders was completed in 2005.

The coils were fabricated by SigmaPhi in Vannes, France, using copper conductor purchased by Jefferson Lab from Phelps-Dodge. The coils are now complete and at the time of writing are on route from France to MIT-Bates. The coil carriers were fabricated by GL&V, Trois-Rivières, PQ and have been delivered to MIT. Small parts machined under TRIUMF supervision by Modern Engineering in Burnaby, BC, and Sunrise Engineering in Delta, BC, are also complete and have been delivered. Mounting straps and fasteners are to be supplied by MIT soon. For the coil and coil-carrier fabrication projects, close supervision and site visits by MIT-Bates and TRIUMF engineers proved to be extremely valuable.

Fabrication of the magnet support structure is under way by B&L in Norfolk, VA under the supervision of Jefferson Lab. The completed stand is to be delivered to MIT-Bates in summer, 2006. Further design engineering and drafting efforts for the support structure rollers, coil alignment fixtures, and dc power and cooling water manifolds are ongoing but these represent straightforward engineering exercises.

The QTOR magnet requires a dc power supply with a capability of 9500 A and 170 V. It was hoped that this could be achieved by modifying the BLAST power sup-

ply at MIT, but that has not proved practical. Power supply bids are now in at Jefferson Lab and a vendor will be selected in early 2006. Initial tests are to be done at MIT-Bates, but unless the Bates electricity contract is changed, running the magnet for even 15 minutes at full power (1.7 MW) could incur a $107,000 demand charge in addition to the energy charge. MIT is investigating different billing schemes with the power vendor.

The Q_{weak} current mode electronics

Overview It is expected that the parity-violating longitudinal analyzing power $A_z \simeq -0.3$ ppm, and it is desired to measure this with a statistical precision of 5×10^{-9} in 2200 hours. To do this requires a count rate of ∼800 MHz in each of the 8 octants. This is too high for conventional pulse counting techniques, so the experiment will operate in current mode. Custom made electronics are now being designed and built at TRIUMF.

Figure 48 shows a block diagram of the Q_{weak} current mode electronics. It consists of low noise transimpedance (current-to-voltage) preamplifiers located in the experimental area and VME based digital integrators, located outside the area. The whole system must be very low noise so that beam-off null asymmetry tests can be made in a short time. Initially, TRIUMF will build a total of 28 dual preamplifiers and 14 octal integrators. Since the modules are of more general utility and can, for example, be used for beam line monitor readout, more will probably be built later.

For certain calibrations it will be necessary to reduce the count rate drastically (by reducing the beam current) and to count individual pulses. To run in this mode we will enter the experimental hall and swap the signal cables from the current mode electronics to the pulse mode electronics.

Noise sources Table V summarizes the sources of noise. The electronics design attempts to keep the electronic noise very low compared to shot noise.

Current to voltage preamplifiers The specifications of the latest TRIUMF preamplifier are:

- Gain: $V_{\rm out}/I_{\rm in} = 1$ MΩ with up to 10 MΩ selectable.
- Output: 0 to 10 V. Adjustable ±2 V offset. Drives 130 m RG-213.
- Input: 10 μA range. Limits depend on offset (e.g. +1 μA to –9μA with one volt offset).
- Bandwidth: $f_{3db} = 30$ kHz (settles to $<10^{-4}$ in 50 μs).
- Density: two amplifiers per module (one module per detector bar).
- Uses 5 V dc supply. Ground fully isolated by internal dc-dc converter.
- BNC connectors
- Small physical size for ease of shielding.

The bandwidth is wide enough to follow a spin flip settling time as short as 50 μs, yet is limited enough to restrict harmonic content to well below the Nyquist frequency of the digital integrator. Figure 49 shows a MK2 prototype. It has switchable gain and reduced

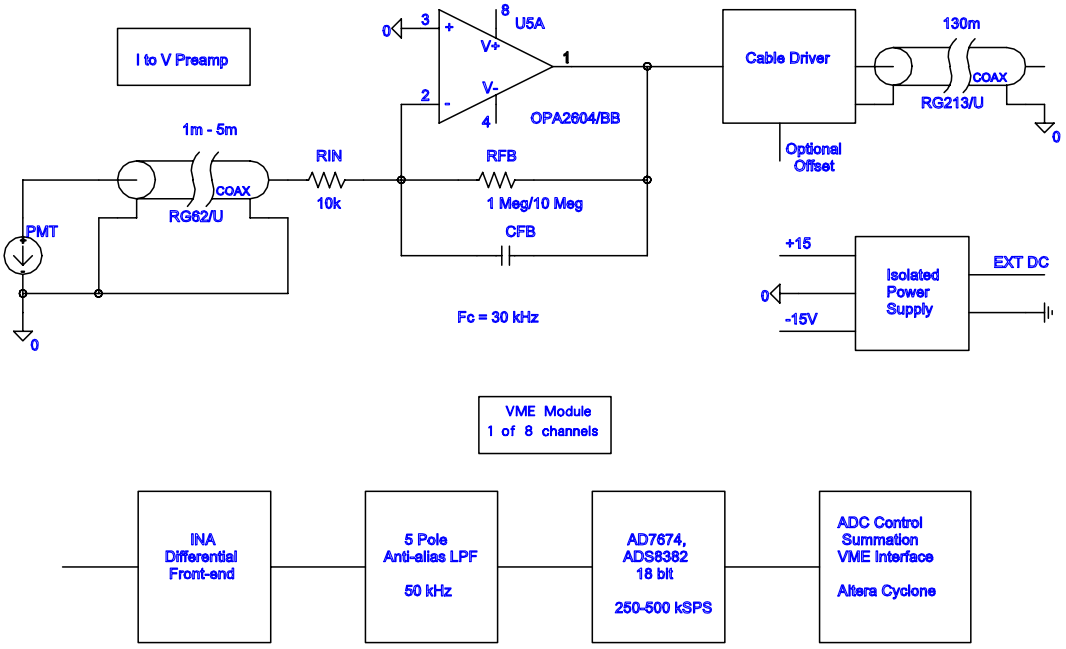

Fig. 48. Block diagram of the Q_{weak} front end electronics. The current to voltage converters are located in the experimental hall and the digital integrators outside, in the electronics cage.

Table V. Noise contributions from different sources.

Condition	Noise on 1/1000 s integral (ppm)
Beam-ON shot noise	1120
Shot noise during LED tests	160
Shot noise during battery tests	5
Preamplifier noise	2
Digital integrator noise	1–2

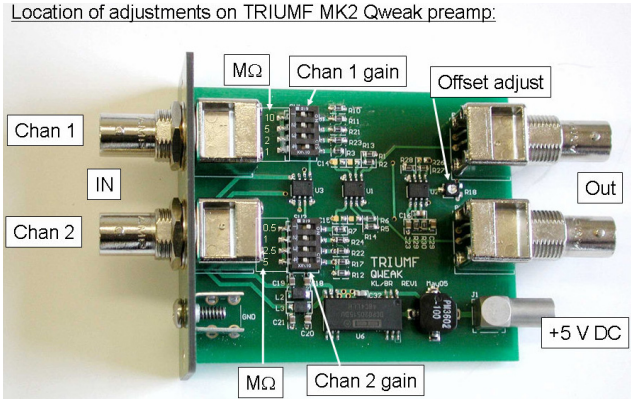

Fig. 49. Layout of the prototype low-noise preamplifier built at TRIUMF. The amplifier was tested for radiation hardness at Jefferson Lab in 2005. There was no noticeable degradation with 18 krad total dose. The specification requires it to tolerate 1 krad.

power supply noise compared to the MK1. The preamplifiers will be placed in Hall C near the main detectors, but shielded as much as possible from radiation. We hope to keep the total dose to the analogue electronics to <1 krad. A MK2 amplifier was tested for radiation hardness at Jefferson Lab. It was subjected to 18 krad total dose at a dose rate of 86 rad/h. No observable change in noise or gain was noticed during or after the radiation.

Noise measurements were made at TRIUMF on a MK2 preamplifier. Table VI shows the noise measurements referred to the amplifier output for different values of input cable capacitance. Note how sensitive the noise is to the capacitance. In practice, the input cable capacitance will be about 275 pf, so the noise will be ∼120 μV. This should be compared to the shot noise of 70,000 μV with the beam on, 10,000 μV if the signal is provided by LEDs, or 300 μV in the best case of a noiseless (except for shot noise) battery.

Table VI. Noise measurements on the MK2 prototype at TRIUMF. Noise measurements were made with a x200, 50 kHz, 5-pole amplifier. The numbers in the table are at the MK2 preamp output.

C_{in} (pf)	Measured (μV)	Pspice (μV)
Open	50	24.4
93	70	51.2
179	100	83.0
275	120	112
726	190	182

Digital integrators To reduce the chance of single event upsets and long term radiation damage, the VME digital signal integrators will be located outside the hall in the Q_{weak} electronics cage. The digital integrator is a VME module with 8 channels of integration per single width VME module. An instrumentation amplifier at the front-end provides common mode noise rejection and is followed by a 50 kHz anti-aliasing filter. An 18 bit ADC operates at a fixed sampling rate up to 800 kSPS. Sampling is controlled by signals derived from external clock and gate signals. The integrator clock will be derived from the 20 MHz Jefferson Lab ion source clock. In response to a trigger (MPS) from the data acquisition system, the module integrates each input for a preset time from 1/300 s to 1/30 s, and delivers the result to the VME interface as four integrals, each 1/4 of the selected integration time. Normally, we expect the integration to be for one 1/250 second spin state, with the result delivered to the VME interface as four, one-millisecond long, integrals. The reason for the short spin states is that it may be difficult to produce a non-boiling liquid hydrogen target that can handle 2 kW, and target boiling data from hall A indicate that the noise from target boiling is limited to low frequencies, with bubbling not seen on a time scale of a few milliseconds.

Averaging of digitization noise The 18-bit ADCs have ∼0.5 LSB rms noise per sample. This "least bit" noise is reduced by averaging ∼500 samples per integration, but the averaging process only works if the raw signal spreads over sufficient ADC channels. With an 18 bit ADC and our proposed analogue bandwidth, the spread should be enough even in the case of a quiet signal. Table VII summarizes the situation.

Table VII. Number of front-end ADC channels covered by the analogue signal for an equivalent noise bandwidth of 47 kHz (f_{3db} = 30 kHz), and an 18 bit ADC at mid-range. Q is the quantum of charge.

Condition	Q (e)	rms noise before integration	Channels (FWHM)
Beam-ON	50,000	69 mV	3339
LED test	1,000	9.8 mV	472
Battery test	1	0.31 mV	15

Compton polarimeter detection system

A measurement of Q_{weak} to 4% requires measuring A_L in polarized electron scattering to the 2% level. To accomplish this an overall uncertainty in P_L to 1% is desired. Using a Möller polarimeter requires interruption of the data collection as it requires reducing the beam to a few μA. It can make a 1% measurement in a short time, but would have to be repeated many times throughout the (long) data-taking run. The solution is to build a Compton polarimeter for Hall C: it can run continuously and non-invasively during the data-taking; it could reach a <1% systematic error over the Q_{weak} experiment; the Möller polarimeter can be used to calibrate it. What is gained is the average current-weighted value for P_L over the Q_{weak} experiment.

Jefferson Lab has decided to proceed with the construction of the required chicane (that will allow for the retention of the present Möller polarimeter), the required laser and beam intersection region, and others will provide the γ detector. The Manitoba/TRIUMF/UNBC/Winnipeg group is requesting NSERC funding to provide detectors of the recoil electrons. In this case, the magnets of the chicane act as a spectrometer and the momentum of the recoil electrons is directly related to their displacement (up to 24 mm with the planned chicane and at the Q_{weak} energy). We intend to measure this with a telescope of four microstrip detectors; by stepping the detectors it should be possible to measure the displacement to 200 μ and help weed-out electrons that are not coming from the intersection region. Measuring the recoil electrons helps to better define the polarimeter acceptance than just using a γ detector alone. This would build directly on the Jefferson Lab Hall A experience which has been successfully operating a Compton polarimeter on the beam line for a few years; thus one can be fairly sure of a successful P_L measurement for Q_{weak}.

A quartz scanner detector for Q_{weak}

The Canadian group is also in the process of proposing to construct a quartz scanner detector for Q_{weak}. The motivation for the detector is:

- to map out the acceptance of the main detectors for the experiment, which are quartz Čerenkov bars, in order to benchmark physics and optics simulations,
- to test linearity of the main detectors with beam current by operating the small detector, which will have similar properties, in pulse-counting mode,
- to scan into the inelastic region, giving greater confidence in any corrections made for inelastic contributions to the asymmetry, and
- to assist in Q^2 determination for the experiment.

The concept and geometry of the scanner is modelled after the similar detector for the SLAC E158 parity-violating Möller scattering experiment. The Q_{weak} scanner would consist of a small quartz radiator residing in an air core light guide, where the light is collected by phototubes.

Monte Carlo studies of the device have begun and indicate sufficient light yield for a geometry consistent with Q_{weak} requirements. Figure 50 shows the rate in MHz in the focal plane for a cm^2 sized detector, at the full Q_{weak} current. The scanner detector is able to map out this shape at any current, independent of the status of the mini-torus magnet, enabling us to achieve the goals listed above. Such Monte Carlo predictions must, however, be confirmed by actual tests. The University of Winnipeg group intends to begin prototyping such a detector, focusing initially on the light yield and timing.

Systematic errors for Q_{weak}

During the past year, a systematic study has been made of the collimator geometry so as to maximize figure of merit while obtaining as clean as possible an image on the Čerenkov bars and acceptably low inelastic rate. With each version of the collimator geometry, the size and shape of the Čerenkov bars has also been modified so as to best intercept the electrons. The maximum size of the collimator was found that would allow electrons to pass through the QTOR magnet without hitting the magnet or support structures. The collimator was then tailored to produce a clean electron image on Čerenkov bars that are 2 m long and 18 cm wide. The image can never be perfect, however, as the

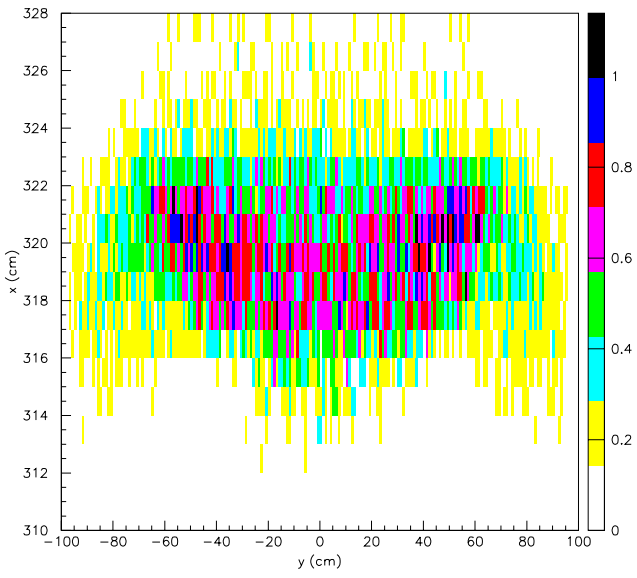

Fig. 50. Expected rates for a 1 cm^2-sized quartz scanner detector in the focal plane of the QTOR magnet (i.e. at the location of the main Čerenkov bars).

radiative tail of the electron distribution extends off the top of the Čerenkov bars, no matter how wide the bar is. The sensitivities to changes of beam properties on helicity flip depend on details of the collimator and on the electron image on the Čerenkov bars and so have to be updated whenever the design of the collimator is changed.

The collimator has been re-designed, and moved from 1.4 m downstream of the target to 2.7 m downstream of the target to improve the sharpness of the electron image at the Čerenkov detector plane, as well as decreasing systematic errors associated with motion of beam on helicity reversal. Systematic errors were reduced due to the reduced size of beam motion relative to the size of the acceptance-defining aperture and by the improved image on the bars. Results are presented here for the final version of the downstream collimator. The aim is for individual sources of systematic error to produce false scattering asymmetries no greater than 6×10^{-9}.

Systematic effects have been modelled with the Q_{weak} GEANT package. To find the effect of beam motion and change of beam size on helicity flip, the event rate on a Čerenkov bar was mapped out as a function of the position (x, y) of a beam element on target. The event rate is well-represented by:

$$R(x, y) = a(1 + bx + cy^2 + dxy^2)$$

over a 2 cm by 2 cm region at the target. Event rate is interpolated with the above fit to the central 4 mm by 4 mm area occupied by the rastered electron beam. The centre of the detector in question lies in the $x - z$ plane and the bar is parallel to the y-axis. The above representation of event rate is applicable to each detector in its own reference frame and so arbitrary motions of the beam on target can be written for each detector bar through suitable rotations.

Beam requirements Table VIII summarizes the requirements to keep the false asymmetries below 6×10^{-9}. In cases where the error goes as a product of quantities, one factor can be traded off against the other. For example, the requirement that the beam be within 0.7 mm of the position neutral axis is based on the assumption that the helicity correlated beam motion is 20 nm. During the $G\emptyset$ experiment the beam motion was only 4 nm. If this were also the case for Q_{weak}, the beam could be up to 3.5 mm off axis. The sensitivity to beam motion is made worse if the experiment lacks perfect octagonal symmetry. In Table VIII, δr is the rms spread in the radial positions of the 8 detector bars and $\delta B/B$ is the fractional rms spread in the magnetic fields of the 8 sectors. The two Requirement columns are for different collimator locations. The Final location offers more relaxed beam parameter constraints.

Effects of offsetting the position of the Čerenkov bars Figure 51 shows a number of parameters as a function of the position of the Čerenkov bars. The horizontal axis shows the distance of the inner edge of the bars from the primary electron beam line. The nominal value is 313 cm. Panel (a) shows the variation of event rate with bar position. The other panels show allowable values of parameters discussed above: (b) x_0 for position modulation; (c) δD for size modulation; (d) the δr requirement for positioning bars relative to each other; (e) $\delta\theta$ for position modulation; and (f) $\delta E/E$ for energy modulation. Although the event rate can be increased slightly by moving the bars out to 315 cm, the beam requirements become tighter.

Detector simulations

Simulations were performed by the Manitoba group to optimize the geometry and rotation angle of the main Q_{weak} quartz Čerenkov detectors. A complete GEANT4 simulation set-up was developed including most major parts of the experiment: target, collimators, magnet, wire chambers, and the main detectors.

Calculations were also performed to estimate errors on Q_W^p and the hadronic contribution (B) using a simulated, Q^2 binned, data set. The goal was to see if the uncertainty in Q_W^p could be reduced by sorting the Q_W^p data according to Q^2.

Simulation set-up The complete simulation set-up is shown in Fig. 52. The collimator geometry for

Table VIII. Beam requirements for false asymmetries of 6×10^{-9} from each individual source. The two Requirement columns are for different collimator locations.

Source of error	Error goes as	Condition	Requirement Final	Requirement Upstream
Position modulation	$x_0\delta x$	$\delta x = 20$ nm	$x_0 < 0.7$ mm	$x_0 < 0.4$ mm
			$\delta r < 19$ mm	$\delta r < 5$ mm
			$\delta B/B < 1.6\%$	$\delta B/B < 0.4\%$
Size modulation	$D_0\delta D$	$D_0 = 200$ μm	$\delta D < 0.4$ μm	$\delta D < 0.24$ μm
Direction modulation	$\theta_0\delta\theta$	$\theta_0 = 60$ μrad	$\delta\theta < 1.4$ μrad	$\delta\theta < 0.4$ μrad
Energy modulation	δE	$E = 1.165$ GeV	$\delta E/E < 6 \times 10^{-9}$	$\delta E/E < 3 \times 10^{-9}$

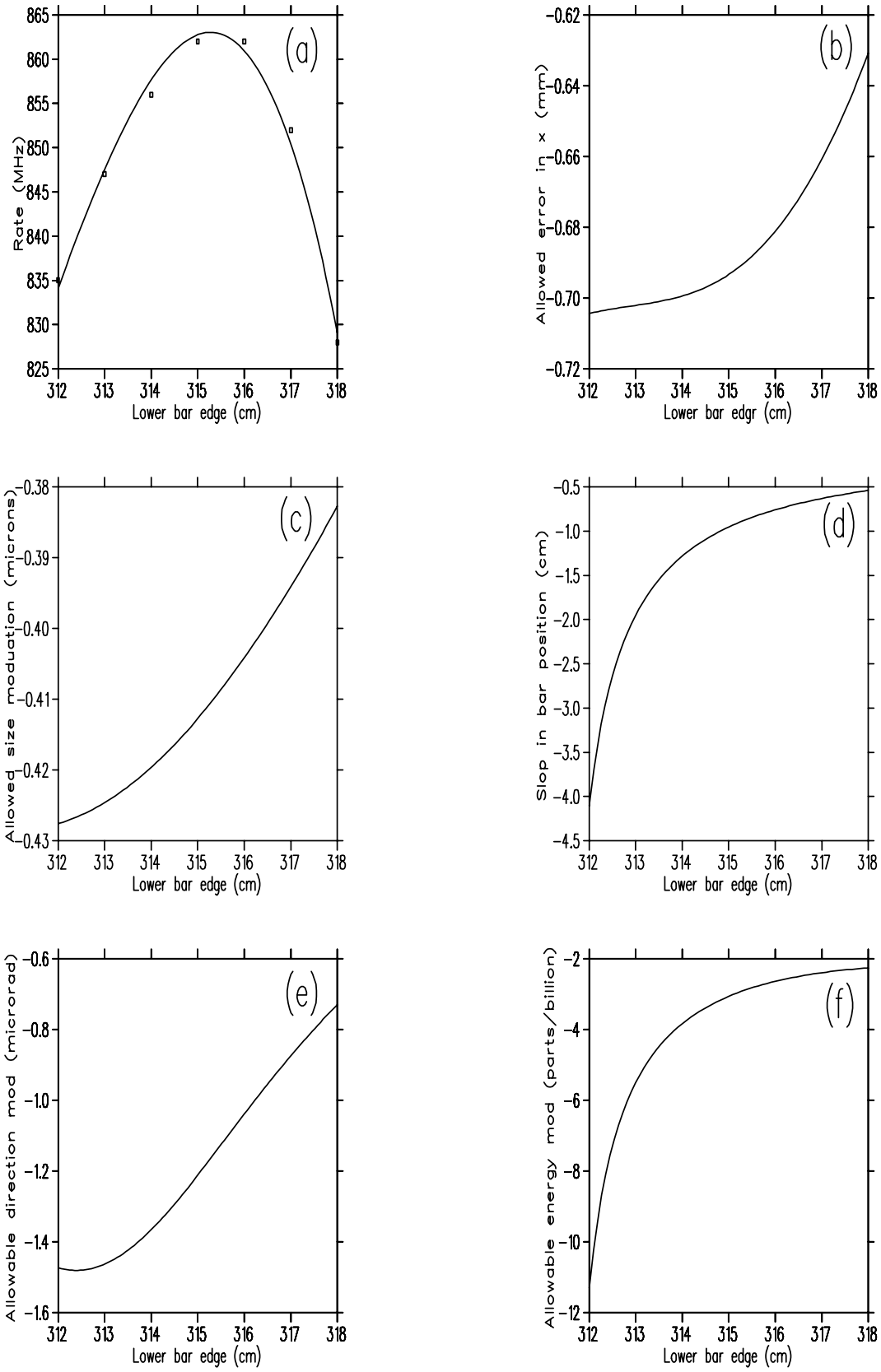

Fig. 51. Event rate as a function of position of the lower edge of a Čerenkov bar, and allowable beam parameters.

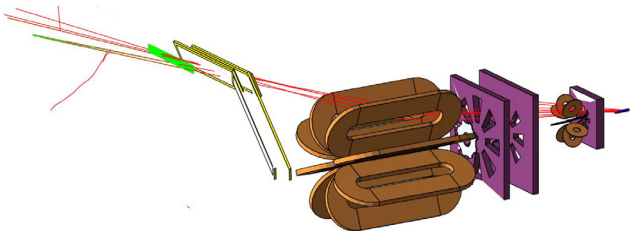

Fig. 52. Current simulation geometry set-up. The collimator set-up is that of the reference design in the 2004 Jeopardy proposal.

this set-up is taken from the reference design in the 2004 Jeopardy proposal. The detector consists of a straight bar, 2 m long and 18 cm wide. (More detailed information about the set-up can be found in K. Grimm's Q_{weak} GEANT4 Simulation log book, http://dilbert.physics.wm.edu/elog/.) The simulations discussed in this Annual Report use only elastic events, using the event data generated by the Q_{weak} GEANT3 code.

The PMT on each side of the Čerenkov bar is modelled by a simple glass surface as the entrance window. In the current set-up the Čerenkov photons for each event are counted as they traverse the boundary between the quartz bar and the PMT entrance window. The mean number of photoelectrons for an event $\langle N_{pe} \rangle$ is calculated by multiplying the total number of counted photons by the quantum efficiency of the particular PMT. The actual number of photoelectrons is then taken from a Poisson distribution with a mean equal to $\langle N_{pe} \rangle$. The quantum efficiencies were obtained from the manufacturer of the PMT.

Detector thickness A thin detector gives less electron shower noise. On the other hand, a thin detector yields less photoelectrons per event, increasing noise from event to event variation. Simulations were performed to determine the optimum Čerenkov detector thickness. The simulation was performed for several different detector thicknesses between 0.5 and 3 cm. For each thickness, 8000 electron hits where recorded across the detector plane.

Figure 53 shows the results of the simulation. Total noise is plotted against thickness for different photocathodes. One sees a shallow minimum in the total noise around 1.0 cm thickness. The actual thickness should be chosen to be a little larger than that, say 1.25 cm, because the number of photoelectrons at 1.0 cm is rather low and allowance also has to be made for light loss in the light guides.

Detector rotation The noise on the signal is affected not only by the thickness of the detector, but also on the tilt angle of the detector relative to the beam. Simulations taking into account the variation in effective detector thickness, the effects of edge events, and the

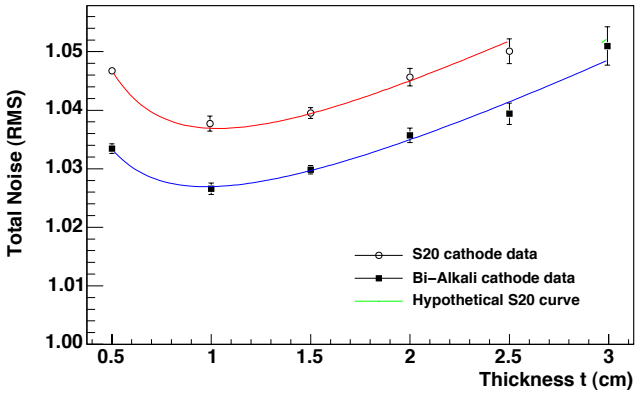

Fig. 53. Total excess noise extracted from simulation for a bialkali (squares) and an S20 (circles) cathode.

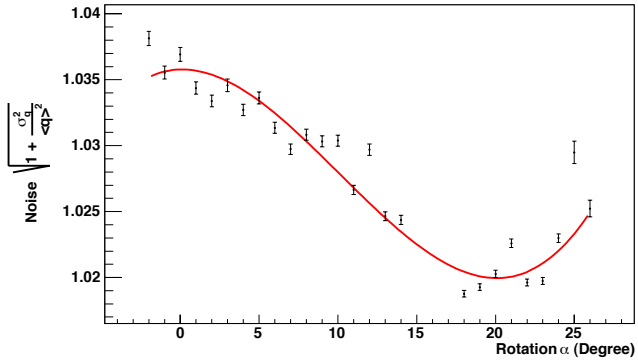

Fig. 54. Overall noise compared to counting statistics, taking into account the noise from the tilt and the signal strength. σ_q^2 is the variance in number of photoelectrons and $< q >$ is the average.

variation in light yield as a function of hit position along the bar indicate that a small tilt angle of between 0 and 5° will minimize the noise. The operating tilt, however, should be that which provides the best signal to noise ratio. Figure 54 shows the final noise compared to counting statistics. The optimum angle is around 20° (bar perpendicular to the electron trajectory).

Q^2 binning effect on Q_W^p and the hadronic corrections At low Q^2, the Q_{weak} physics asymmetry is related to the proton weak charge and its hadronic form factor contribution by:

$$A = k \left[Q^2 Q_w^p + Q^4 B \right] ,$$

where, for simplicity, the hadronic form factor B is assumed to be Q^2 independent, which is quite accurate for $Q^2 \lesssim 0.1$ GeV^2. The Q_{weak} experiment intends to measure a single asymmetry, averaged over the range of momentum transfer $Q^2 \simeq 0.01 \rightarrow 0.09$ GeV^2, with a cross section weighted average momentum transfer of 0.03 GeV^2. This Q^2 is low enough to reduce the effect of the $Q^4 B$ term, but not so low as to make the asymmetry too small to measure.

Simulations were performed to study whether sorting the data by Q^2 would permit an improved correction for the hadronic term over what could be obtained by depending on already published data alone.

Such a Q^2 binning could, in principle, be achieved by constructing additional detectors some distance behind the current position of the Čerenkov detectors. For example, to separate the Q_{weak} range into 5 bins it would be necessary to have 5 additional detectors located about 3 m downstream of the Čerenkov detectors. Figure 55 shows how the events are dispersed according to Q^2 at 3 m downstream of the focal plane.

For the study, the total yield was separated evenly into eight regions between Q^2 = 0.01 GeV^2 and Q^2 = 0.09 GeV^2, with a Q^2 value for each bin taken from the bin middle. The extracted values for Q_w^p and B are then separately histogrammed and their respective errors are taken from the histogram RMS widths. Some of the calculations were changed slightly. For example, sometimes a third fit parameter, in the form of a Q^2 independent (offset asymmetry) term was introduced to investigate the effect on the Q_w^p and B errors.

Some of the calculations also included an additional data point at $Q^2 = 0.1$ GeV^2 with an error bar of 3.5%. The additional data point is an attempt to include the constraints imposed by hadronic form factor data from other experiments at higher Q^2. The 3.5% error on this data point was obtained by fitting the existing and projected world database and includes only the error corresponding to the hadronic asymmetry.

Results were obtained for eight different fits with varying parameters and including both "pure" simulated data as well as simulated data in combination with the additional data point at $Q^2 = 0.1$ GeV^2.

Two main conclusions were drawn from the simulations. First, and perhaps most important, is that averaging over the large range in momentum transfer produces no great loss in the accuracy of the measured asymmetry. Second, we find that a Q^2 binned Q_{weak} data set would reduce the error on Q_w^p by about 10%. However, even this relatively small reduction is likely unrealizable, due to detector size limitations, and the construction of additional detectors is not justified. For the data range included here and the simple form for the asymmetry that was used, Q_w^p and B are highly anti-correlated and a more complete world data set

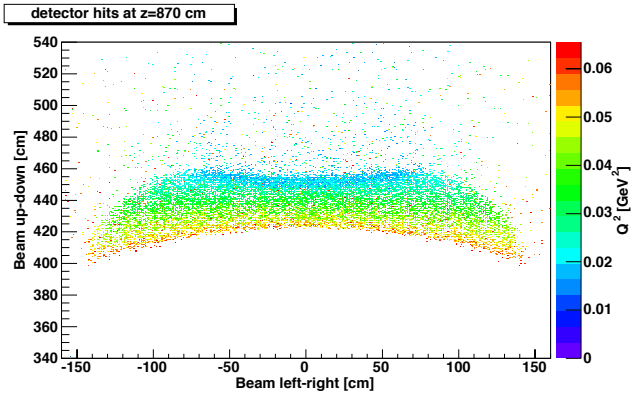

Fig. 55. Event distribution by Q^2 at z = 870 cm, 3 m downstream of the focal plane. The correlation between Q^2 and vertical position is evident.

needs to be included to improve the fit. However, using more of the world data at higher Q^2 values requires a more complicated fit function with more parameters which could possibly reduce the correlation.

List of Q_{weak} collaborators: M.J. Ramsey-Musolf, Caltech; D. Armstrong, T. Averett, J.M. Finn, K.H. Grimm, College of William and Mary; T. Smith, Dartmouth College; C. Keppel, Hampton University; P. Bosted, A. Bruell, R.D. Carlini, S. Chattopadhyay, R. Ent, D.J. Gaskell, A. Lung, D. Mack, S. Majewski, D. Meekins, M. Poelker, J. Roche, G.R. Smith, S. Wood, C. Zorn, Jefferson Lab; J.D. Bowman, G. Mitchell, S. Penttila, W.S. Wilburn, Los Alamos National Lab; T. Forest, K. Johnston, N. Simicevic, S. Wells, Louisiana Technical University; J.A. Dunne, Mississippi State University; T. Botto, K. Dow, M. Farkhondeh, W. Franklin, M. Khol, S. Kowalski, Y. Prok, E. Tsentalovich, T. Zwart, MIT; V. Ziskin, MIT-Bates Linear Accelerator; Y. Liang, A.K. Opper, Ohio University; C.A. Davis, J. Doornbos, TRIUMF; J. Erler, Universidad Nacional Autonoma de Mexico; R. Jones, K. Joo, University of Connecticut; J. Birchall, A. Coppens, W.R. Falk, M. Gericke, L. Lee, S.A. Page, W.D. Ramsay, W.T.H. van Oers, University of Manitoba; S. Covrig, F.W. Hersman, M. Holtrop, H. Zhu, University of New Hampshire; E. Korkmaz, T. Porcelli, University of Northern BC; J. Martin, University of Winnipeg; J. Mammei, R. Mammei, N. Morgan, M. Pitt, R. Suleiman, Virginia Polytechnic Institute; H. Mkrtchyen, Yerevan Physics Institute. Experiment status: in preparation.